
















JWST Detection of Hydrocarbon Ices and Methane Gas on Makemake

SILVIA PROTOPAPA ¹, IAN WONG ², EMMANUEL LELLOUCH ³, PERIANNE E. JOHNSON ⁴, WILLIAM M. GRUNDY ^{5,6},
CHRISTOPHER R. GLEIN ⁷, THOMAS MÜLLER ⁸, CSABA KISS ^{9,10,11}, JOSHUA P. EMERY ⁶, ROSARIO BRUNETTO ¹²,
BRYAN J. HOLLER ², ALEX H. PARKER ¹³, JOHN A. STANSBERRY ², HEIDI B. HAMMEL ¹⁴, STEFANIE N. MILAM ¹⁵,
AURÉLIE GUILBERT-LEPOUTRE ¹⁶, PABLO SANTOS-SANZ ¹⁷ AND NOEMÍ PINILLA-ALONSO ^{18,19}

¹*Southwest Research Institute, Boulder, CO, USA*

²*Space Telescope Science Institute, Baltimore, MD, USA*

³*LIRA, Observatoire de Paris, PSL Research University, CNRS, Sorbonne Université, Meudon, France*

⁴*University of Texas Institute for Geophysics, Austin, TX, USA*

⁵*Lowell Observatory, Flagstaff, AZ, USA*

⁶*Northern Arizona University, Flagstaff, AZ, USA*

⁷*Southwest Research Institute, San Antonio, TX, USA*

⁸*Max-Planck-Institut für extraterrestrische Physik, Garching, Germany*

⁹*Konkoly Observatory, HUN-REN Research Centre for Astronomy and Earth Sciences, Budapest, Hungary*

¹⁰*CSFK, MTA Centre of Excellence, Budapest, Hungary*

¹¹*ELTE Eötvös Loránd University, Institute of Physics and Astronomy, Budapest, Hungary*

¹²*Université Paris-Saclay, CNRS, Institut d'Astrophysique Spatiale, Orsay, France*

¹³*SETI Institute, Mountain View, CA, USA*

¹⁴*Association of Universities for Research in Astronomy, Washington, DC, USA*

¹⁵*NASA Goddard Space Flight Center, Greenbelt, MD, USA*

¹⁶*LGL-TPE, CNRS, Université Lyon 1, ENSL, Villeurbanne, France*

¹⁷*Instituto de Astrofísica de Andalucía, CSIC, Granada, Spain.*

¹⁸*Institute of Space Science and Technology of Asturias (ICTEA), University of Oviedo, Oviedo, Spain*

¹⁹*Department of Physics, University of Central Florida, Orlando, FL, USA*

ABSTRACT

JWST/NIRSpec observations of Makemake reveal a chemically complex surface and evidence of gaseous CH₄. Our spectral modeling indicates a surface composition consisting of CH₄, CH₃D, and possibly CH₃OH, combined with aggregates of C₂H₂ and C₂H₆. The presence of C₂H₄ is also considered given its expected photochemical origin. Both areal and layered configurations reproduce the observed spectrum, with the latter being preferred. This composition confirms earlier hydrocarbon detections and suggests that CH₄ photolysis is either ongoing or occurred recently. The detection of CH₃D yields a D/H ratio in CH₄ ice of $(3.98 \pm 0.34) \times 10^{-4}$, consistent within 2σ with previous estimates. We report the first detection of CH₄ fluorescence from Makemake, establishing it as only the second trans-Neptunian object—after Pluto—with confirmed volatile release. We explore two scenarios consistent with the observed CH₄ emission, though neither fully reproduces the data: an expanding coma, yielding production rates of $(0.2\text{--}1.6) \times 10^{28}$ molecules s^{−1} and a rovibrational temperature of ~ 35 K, possibly originating from a localized plume, and a gravitationally bound atmosphere, which, if adopted, implies gas kinetic temperatures near 40 K and surface pressures of ~ 10 pbar—values consistent with stellar occultation constraints and an atmosphere in equilibrium with surface CH₄ ice. Discriminating between these scenarios will require higher spectral resolution and improved signal-to-noise observations. Together, the gas-phase CH₄, intermediate D/H ratio between that in water and CH₄ in comets, and complex surface composition challenge the traditional view of Makemake as a quiescent, frozen body.

Keywords: Dwarf planets (419) — Infrared spectroscopy (2285) — Ice spectroscopy (2250) — Molecular spectroscopy (2095) — James Webb Space Telescope (2291)

1. INTRODUCTION

Makemake, also known as 2005 FY₉, has a spherical-equivalent diameter of ~ 1430 km and a high geometric albedo of $p_V \sim 0.8$ (J. L. Ortiz et al. 2012; M. E. Brown 2013; T. A. Hromakina et al. 2019). Its near-infrared spectrum is dominated by strong methane (CH₄) absorption bands that appear broad and, in some instances, saturated (M. E. Brown 2012, and references therein)—markedly different from those observed on other volatile-rich trans-Neptunian objects (TNOs). Stellar occultation measurements revealed the absence of a global Pluto-like atmosphere, with a 1σ upper limit of 4–12 nbar at the surface (J. L. Ortiz et al. 2012). This result was interpreted by J. L. Ortiz et al. (2012) as evidence for a strong depletion of nitrogen (N₂) ice, whose vapor pressure exceeds the microbar level at surface temperatures above ~ 33.6 K (N. Fray & B. Schmitt 2009)—a temperature that is plausible for Makemake, depending on the adopted albedo and phase integral.

Observations obtained with the JWST Near-Infrared Spectrograph (NIRSpec) covering the 3.9–4.8 μm range confirmed the presence of solid CH₄ and placed tight upper limits on solid N₂ and carbon monoxide (CO) at 3% and 1 ppm, respectively (W. M. Grundy et al. 2024a). These results are consistent with earlier constraints from stellar occultations and support the interpretation that Makemake’s surface is dominated by CH₄ and strongly depleted in N₂ and CO. The same dataset revealed the presence of the CH₃D isotopologue, enabling the first measurement of the deuterium-to-hydrogen (D/H) ratio in CH₄ ice on a TNO. The origin of Makemake’s CH₄ remains debated: geochemical modeling suggests it may be produced internally through water–rock interactions or abiotic organic synthesis and subsequently released via outgassing or cryovolcanism (C. R. Glein et al. 2024), while alternative models favor the incorporation of primordial CH₄ from the protosolar nebula (O. Mousis et al. 2025).

Methane-rich surfaces exposed to ultraviolet radiation and energetic particles undergo chemical evolution, leading to the formation of more complex hydrocarbons (e.g., C. J. Bennett et al. 2006). Ethane (C₂H₆), a product of CH₄ irradiation, was first detected on Makemake by M. E. Brown et al. (2007), and higher spectral resolution observations later revealed solid ethylene (C₂H₄), acetylene (C₂H₂), and higher-mass alkanes (M. E. Brown et al. 2015). These products trace the irradiation pathway from CH₄ to long-chain hy-

drocarbons. Makemake’s lack of N₂ allows CH₄ to dominate its surface and may enhance the efficiency of irradiation-driven reactions in the absence of significant atmospheric shielding.

In addition to these compositional insights, observations of Makemake with Spitzer, Herschel, and JWST’s Mid-Infrared Instrument revealed a strong mid-infrared (18–25 μm) excess, corresponding to temperatures near 150 K—well above those expected from solar insolation alone. Proposed explanations include a small thermally active region (with an equivalent radius of 10.0 ± 0.5 km, or $\sim 0.02\%$ of Makemake’s apparent disk), potentially associated with cryovolcanism, or a previously undetected ring composed of fine carbonaceous dust (C. Kiss et al. 2024). Although stellar occultation measurements do not rule out localized outgassing, no direct evidence of such activity has been observed to date.

These recent observations have revealed intriguing characteristics of Makemake, making it a prime target for further investigation to explore its volatile inventory and provide additional insights into the surface evolution of large, distant icy worlds. Here, we present JWST/NIRSpec observations of Makemake spanning 1.0–4.8 μm , with the aim of characterizing its surface composition, identifying irradiation products of CH₄, and assessing possible spectroscopic indicators of activity. These observations expand upon previous analyses by providing the first view of Makemake across the entire NIRSpec wavelength range.

2. OBSERVATIONS AND DATA REDUCTION

Makemake was observed with the integral field unit (IFU) on JWST/NIRSpec as part of Cycle 1 Solar System Guaranteed Time Observations program #1254. The IFU mode provides a $3.0'' \times 3.0''$ field of view at a spatial sampling of 0.1'' per pixel. Observations used the medium-resolution gratings G140M, G235M, and G395M, paired with the F100LP, F170LP, and F290LP filters, covering wavelength ranges of 1.0–1.8, 1.7–3.1, and 2.9–5.1 μm , respectively, at a spectral resolving power of $\lambda/\Delta\lambda \sim 1000$ (T. Böker et al. 2023). Full observational details are provided in Appendix A (see also Table 1).

The results presented in this Letter rely on spectra extracted via a point spread function (PSF) fitting technique, with a fixed centroid position and empirically derived PSF models (see details in Appendix A). This method provided the highest signal-to-noise ratio. The

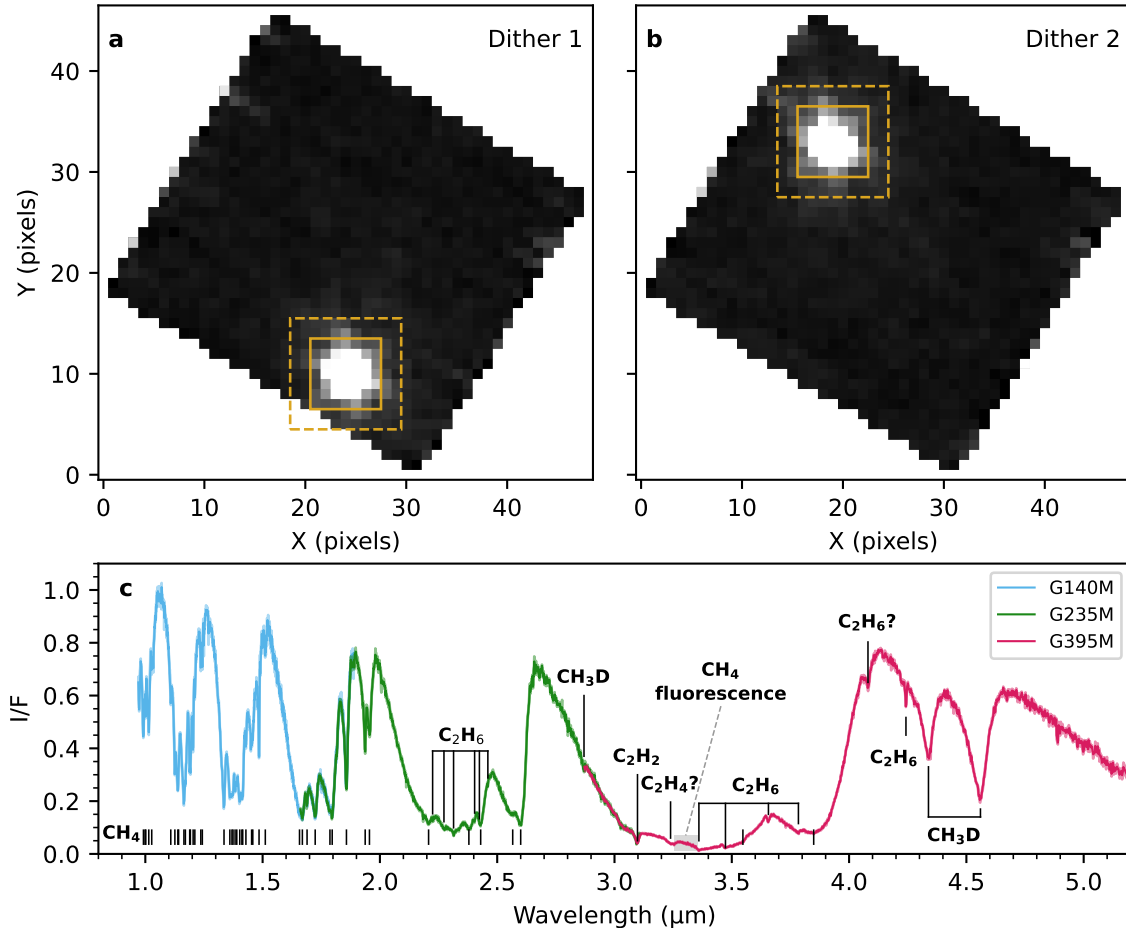


Figure 1. JWST/NIRSpec IFU observations of Makemake and detected species. Panels (a) and (b) show the median images from the two dither positions acquired with the G235M grating, collapsed along the wavelength axis. The 7×7 pixel extraction aperture (solid gold box) and the 11×11 pixel region used as the inner boundary to characterize the background (dashed gold box) are overlaid. Panel (c) presents the extracted reflectance spectra from the G140M, G235M, and G395M gratings. The spectra show excellent agreement in the overlapping wavelength regions, confirming the consistency of the extraction and calibration procedures. The ice species attributed to the detected absorption bands in Makemake’s spectrum, as well as the region of CH_4 fluorescence, are labeled.

individual spectra from the two dithered exposures were averaged, corrected for flux losses using observations of the standard star P330-E acquired with the same instrumental configuration, and converted to reflectance (I/F) using Makemake’s known size (radius $R = 715$ km) and viewing geometry at the time of observation (heliocentric distance $r_h = 52.6$ AU, observer–target distance $\Delta = 52.2$ AU). Outliers were then masked using relative error filtering to produce the final combined spectrum.

The 7×7 pixel spectral extraction aperture and the 11×11 pixel inner boundary of the background region are shown in panels (a) and (b) of Figure 1. The resulting spectra from each grating, presented in panel (c), show excellent agreement in the overlapping wavelength regions, demonstrating the consistency of the extraction and calibration procedures across the spectral settings.

3. SURFACE COMPOSITION

We performed radiative transfer modeling of Makemake’s full $1.0\text{--}4.8$ μm JWST/NIRSpec spectrum to investigate its surface composition, quantify the abundances of hydrocarbon species, and place improved constraints on the D/H ratio. Our analysis focused on diagnostic vibrational absorption bands of solid CH_4 , its isotopologue CH_3D , and additional features attributed to more complex hydrocarbons. We adopted the Hapke radiative transfer model (B. Hapke 1993, 2002, 2012) and explored a range of physically motivated configurations—intimate mixtures, areal mixtures, and stratified (layered) geometries—to account for plausible surface compositional heterogeneity (see Appendix B for details). The free parameters in the model include the optical path length (D , used as a proxy for grain size);

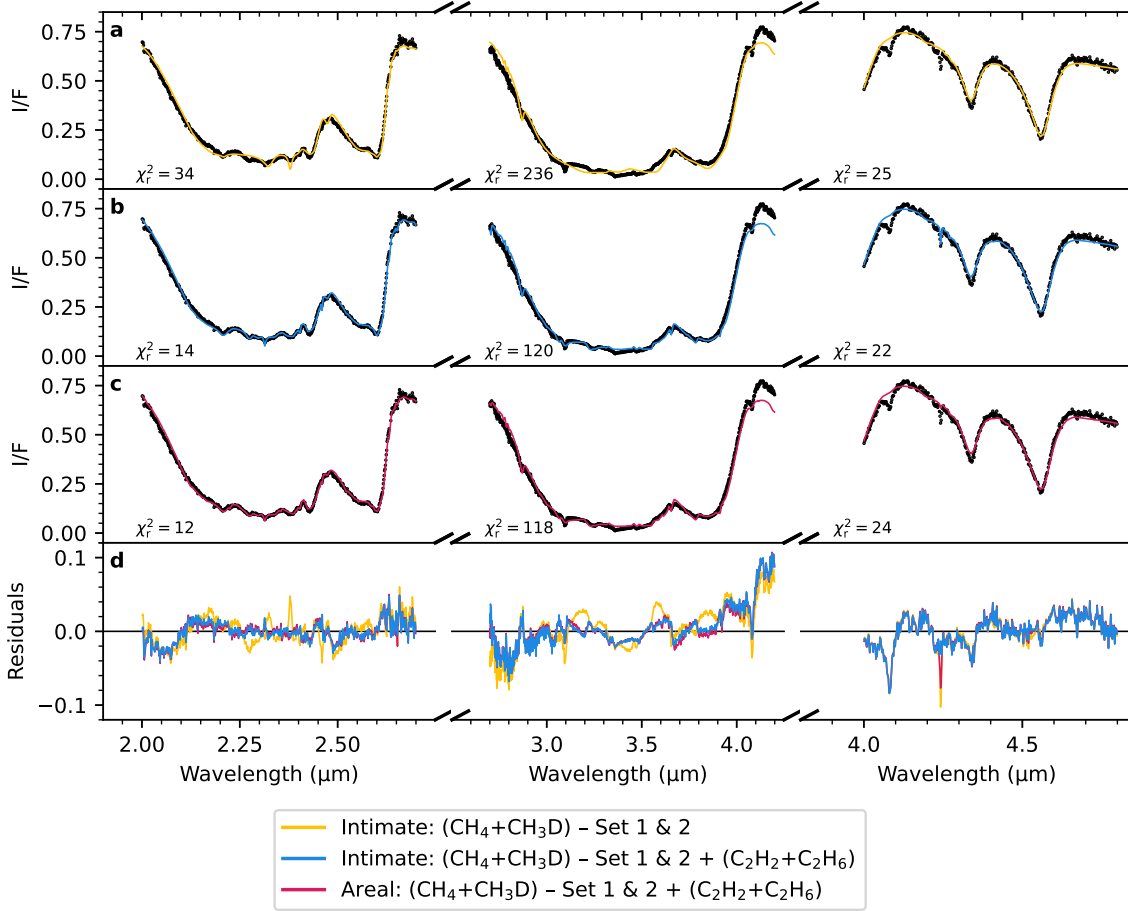


Figure 2. Spectral modeling of Makemake over short, medium, and long wavelength ranges. Panels (a)–(c) compare the observed JWST spectrum (black points) to three compositional models: (a) a baseline model including only two intimately mixed sets of CH₄ + CH₃D, (b) an intimate mixture of CH₄ + CH₃D with an added C₂H₂ + C₂H₆ aggregate, and (c) an areal mixture with the same components as in (b). Each segment corresponds to a distinct wavelength interval—short (2.0–2.7 μm), medium (2.7–4.2 μm), and long (4.1–4.8 μm)—that was modeled independently. Panel (d) shows residuals for all models across the corresponding wavelength range. The addition of C₂H₂ + C₂H₆ substantially improves the fit in all three intervals, strongly supporting the presence of these species on Makemake’s surface, regardless of mixing geometry.

the abundance of each compound, expressed as fractional area (F) or volume (V), depending on the mixing geometry; the D/H ratio; and, for aggregates, the relative volume fractions of the constituents. For layered configurations, an additional free parameter is the optical thickness of the uppermost layer, τ .

3.1. Modeling-based Identification of Surface Ices

A stepwise modeling analysis was applied to evaluate the molecular inventory required to reproduce the observed spectral features and disentangle the individual contributions of each species. All models included two CH₄ + CH₃D components, constrained to share a common D/H ratio but allowed to vary independently in abundance and path length. This baseline setup was first tested on its own, followed by the addition of an aggregate composed of C₂H₆ (R. Mastrapa, private com-

munication; see Appendix C.2) and C₂H₂ (R. L. Hudson et al. 2014a, crystalline phase at 40 K). Modeling was initially performed independently over three distinct wavelength intervals—short (2.0–2.7 μm), medium (2.7–4.2 μm), and long (4.1–4.8 μm)—to isolate specific absorption bands and minimize parameter degeneracy.

Across the short and medium wavelength ranges, the inclusion of a C₂H₂ + C₂H₆ aggregate significantly improved the fit relative to models containing only CH₄ + CH₃D, decreasing the reduced chi-squared statistic (χ_r^2) by a factor of 2–3. Although C₂H₂ and C₂H₆ were also evaluated as separate components, the aggregate configuration consistently yielded superior fits. Although C₂H₂ and C₂H₆ were also evaluated as separate components, those configurations consistently yielded higher χ_r^2 values and failed to reproduce key spectral features observed in the data, such as the narrow 3.1-μm ab-

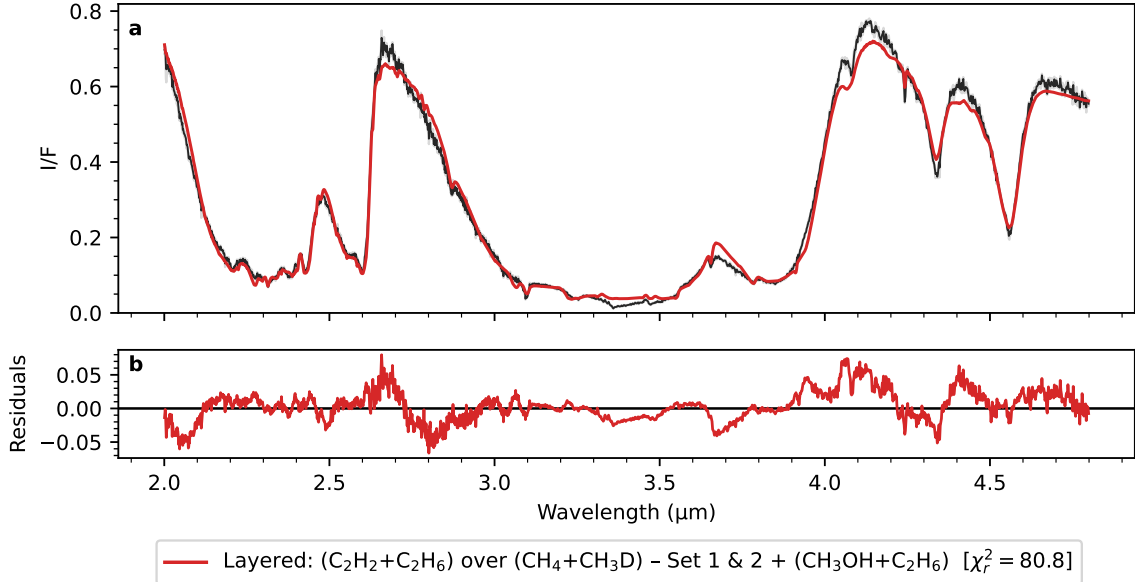


Figure 3. Best-fit spectral model of Makemake from 2.0–4.8 μm . The observed JWST/NIRSpec spectrum (black line) is shown with 1σ uncertainties as a shaded gray envelope. The best-fit model (red line) corresponds to a layered configuration (F-Layered-4; see Table 2) in which a $\text{C}_2\text{H}_2 + \text{C}_2\text{H}_6$ aggregate overlies two $\text{CH}_4 + \text{CH}_3\text{D}$ components and a $\text{CH}_3\text{OH} + \text{C}_2\text{H}_6$ aggregate. This configuration simultaneously reproduces the continuum shape and major absorption features, including bands attributed to CH_4 , CH_3D , C_2H_2 , and C_2H_6 . While no distinct CH_3OH absorption features are clearly identified, its inclusion facilitates an accurate reproduction of the continuum across the entire spectral range. The model also enables a consistent estimate of the D/H ratio across plausible configurations. Residuals are shown in the bottom panel.

sorption band. Areal and intimate mixing geometries perform comparably. From a statistical standpoint, the areal configuration provides a better fit in the short and medium wavelength ranges, whereas the intimate configuration is favored in the long range. At this stage, χ_r^2 was used solely as a relative metric, with the models serving primarily as a first diagnostic step to evaluate the relative importance of different compounds rather than to achieve an exact match to the data. From this relative assessment, the inclusion of a $\text{C}_2\text{H}_2 + \text{C}_2\text{H}_6$ aggregate is clearly required to reproduce the observed spectral features, while it is not possible to discriminate between areal and intimate mixing geometries. These results are illustrated in Figure 2 and summarized in Appendix B, Table 2 (first nine rows), which compiles the full suite of models explored, along with their configurations, fit quality, and retrieved D/H values.

With the $\text{C}_2\text{H}_2 + \text{C}_2\text{H}_6$ aggregate established as a necessary component in the range-specific fits, we extended the modeling to the full 2.0–4.8 μm wavelength range to assess compositional models across the entire spectrum. The lower bound of 2.0 μm was selected based on the availability of reliable optical constants for the relevant hydrocarbons. Although the combination of two $\text{CH}_4 + \text{CH}_3\text{D}$ components and a $\text{C}_2\text{H}_2 + \text{C}_2\text{H}_6$ aggregate provides an adequate description of the observed spectral features when evaluated over individual wavelength

intervals, the corresponding full-range areal model (F-Areal-2) underestimates the strength of the absorption bands between 2.1 and 2.6 μm and fails to reproduce the narrow 3.1- μm feature. Its intimate counterpart (F-Intimate-2) exhibits similar shortcomings, indicating that this composition alone cannot account for the observed continuum and fine-scale structure across the entire spectral range (see Table 2 and Figure 6, both in Appendix B).

To explore alternative physically motivated geometries, we tested a layered configuration with $\text{C}_2\text{H}_2 + \text{C}_2\text{H}_6$ overlying $\text{CH}_4 + \text{CH}_3\text{D}$. This arrangement is consistent with the formation of C_2H_2 and C_2H_6 as radiolytic or photolytic by-products of surface CH_4 . However, the layered configuration alone is insufficient to reproduce the continuum (see Table 2, model F-Layered-2).

An additional component is therefore required. We evaluated several candidates—including tholin-like materials, amorphous carbon, pyroxene, C_2H_4 , and methanol (CH_3OH , crystalline form at 120 K; P. A. Gerakines & R. L. Hudson 2020)—and found that only models incorporating CH_3OH significantly improved the fit, reducing χ_r^2 by a factor of ~ 1.7 relative to models without CH_3OH . Intimate mixtures containing CH_3OH exhibited strong parameter degeneracies and poor convergence (see Appendix B) and are therefore not included

in Table 2. Based on visual inspection, satisfactory fits were obtained with either (1) an areal mixture composed of CH_3OH , two $\text{CH}_4 + \text{CH}_3\text{D}$ components, and $\text{C}_2\text{H}_2 + \text{C}_2\text{H}_6$, or (2) a layered structure in which $\text{C}_2\text{H}_2 + \text{C}_2\text{H}_6$ overlies $\text{CH}_4 + \text{CH}_3\text{D}$ and either CH_3OH or a $\text{CH}_3\text{OH} + \text{C}_2\text{H}_6$ aggregate (models F–Areal–3, F–Layered–3, and F–Layered–4, respectively). These configurations reproduce both the observed continuum and major absorption features (Figures 3 and 6) and yield Markov Chain Monte Carlo (MCMC) solutions with good convergence (see Appendix B and Figures 7 and 8 for the full posterior distributions).

Despite these improvements, all full-range models retain elevated χ_r^2 values, indicating residual spectral structure not fully captured by the current parameterizations. This could reflect uncertainties in the adopted optical constants, the presence of additional spectral components, or an underestimation of observational errors. To assess the impact of underestimated observational errors and other unmodeled sources of variance, we inflated the errors by a factor of 9 to bring the χ_r^2 of the F–Areal–3 fit to unity and applied this same factor to all full-range models before repeating the MCMC runs. The resulting parameter estimates were consistent with those from the nominal fits, but the credible intervals broadened by roughly an order of magnitude, indicating that the uncertainties reported for the unscaled fits should be regarded as lower limits.

To clarify the role of individual compounds in shaping the observed spectrum, we constructed a decomposition based on the areal mixture model F–Areal–3, which includes the same molecular components as other configurations. The top row of Figure 4 compares the observed JWST/NIRSpec spectrum to synthetic models generated using two components of either $\text{CH}_4 + \text{CH}_3\text{D}$ or CH_4 alone. The inclusion of CH_3D is essential to reproduce the doublet structure in the long-wavelength region (4.3–4.6 μm) and weaker combination bands at 2.47 and 2.87 μm , marked by dashed blue lines in panels (a)–(c).

The bottom row shows residuals after subtracting the $\text{CH}_4 + \text{CH}_3\text{D}$ model from the observed spectrum, along with scaled synthetic spectra of $\text{C}_2\text{H}_2 + \text{C}_2\text{H}_6$, C_2H_6 alone, CH_3OH , and C_2H_4 . The strong absorption at 3.1 μm is particularly diagnostic of C_2H_2 and plays a central role in constraining its abundance. Several C_2H_6 bands at 2.2–2.5, 3.3–3.8, and near 4.2 μm correspond to residual features not explained by $\text{CH}_4 + \text{CH}_3\text{D}$ alone. Although CH_3OH lacks strong, isolated bands, its inclusion significantly reduces the overall χ_r^2 value (from ~ 130 to ~ 80) and improves the continuum match—particularly by suppressing the upward curvature visible in the residual spectrum beyond 3.5 μm , as shown in the

bottom row of Figure 4. Among the compounds considered, only CH_3OH exhibits the broad, continuum-like absorption needed to account for this feature. However, due to the absence of distinct diagnostic bands, we cannot exclude the possibility that another compound with similar spectral behavior could produce a comparably good fit. Thus, the identification of CH_3OH remains tentative.

C_2H_4 introduces minor features that partially overlap with those of C_2H_6 , but when included in the full mixture, its best-fit abundance consistently converges to zero. It is therefore excluded from the final model. Nonetheless, its presence is chemically expected, as it shares the same photochemical production pathways as C_2H_6 . In addition, the C_2H_6 optical constants adopted in our modeling exhibit a broad absorption feature near 3.2–3.3 μm that could partially overlap with C_2H_4 bands. While comparisons with other C_2H_6 and C_2H_4 datasets do not yield a definitive conclusion (Appendix C.2), this raises the possibility that a contribution from C_2H_4 is already embedded in the C_2H_6 spectrum. In that case, the modeling would not attribute any separate abundance to C_2H_4 unless its spectral signature were explicitly disentangled from that of C_2H_6 —a separation that is currently not feasible given the ambiguity in available laboratory data.

3.2. Constraints on the D/H Ratio in CH_4 Ice

The strongest CH_3D absorption bands occur in the long-wavelength region (4.2–4.8 μm), making this interval particularly diagnostic for estimating the D/H ratio in CH_4 ice. Within this range, modeling the spectrum with only $\text{CH}_4 + \text{CH}_3\text{D}$ reproduces the CH_3D band shapes well and yields a D/H ratio of 3.62×10^{-4} (Table 2, model L–Intimate–1). However, other species—especially C_2H_6 and C_2H_2 —introduce overlapping features, such as the C_2H_6 band at 4.24 μm , that partially blend with CH_3D . Accounting for these absorbers modifies the retrieved D/H ratio; for example, including C_2H_6 and C_2H_2 in the L–Intimate–2 model lowers the estimate to 3.54×10^{-4} . This shift reflects both spectral blending and the interdependence of abundance and path length in multicomponent models: adding an absorber alters the relative contributions of all species to the total absorption, thereby affecting their best-fit parameters and the resulting D/H value. This demonstrates the importance of properly modeling all contributing absorbers when retrieving D/H ratios.

Although the long-wavelength interval is the most sensitive to CH_3D , broader wavelength coverage strengthens these constraints: CH_3D exhibits additional, albeit weaker, features at shorter wavelengths, and fitting

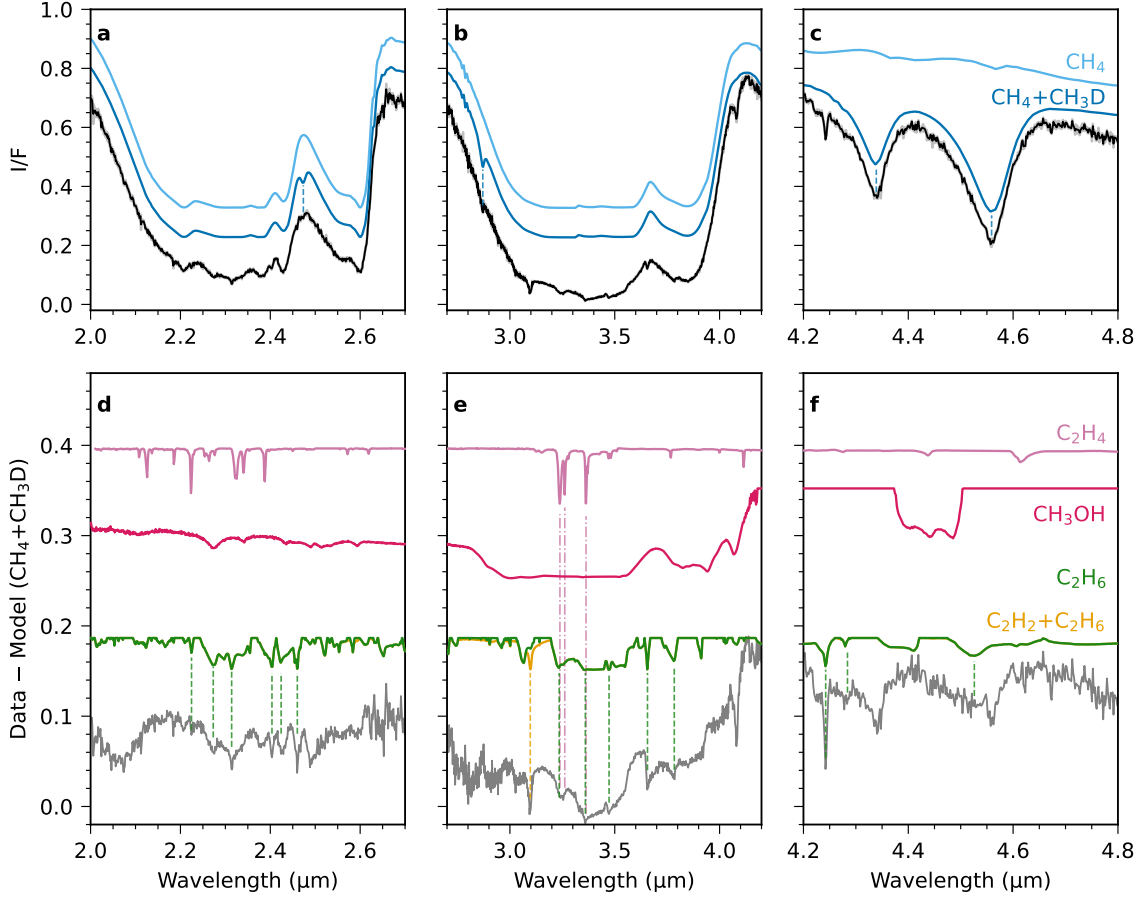


Figure 4. Contribution of individual molecular components to the observed JWST/NIRSpec spectrum of Makemake. Top row: comparison between the observed spectrum (black) and synthetic spectra of CH_4 alone (cyan) versus $\text{CH}_4 + \text{CH}_3\text{D}$ (blue), with a shared D/H ratio. Key CH_3D features at 2.47, 2.87, 4.34, and 4.56 μm are indicated by vertical dashed lines. Bottom row: residuals after subtracting the $\text{CH}_4 + \text{CH}_3\text{D}$ model (gray), shown alongside scaled synthetic spectra of $\text{C}_2\text{H}_2 + \text{C}_2\text{H}_6$ (orange), C_2H_6 alone (green), CH_3OH (red), and C_2H_4 (pink). Distinctive absorption bands and continuum profiles help identify the presence or absence of these species (see text for details).

the full 2.0–4.8 μm range improves the robustness of the solution (Figure 4). The most reliable D/H values are therefore those retrieved from full-range models—F-Areal-3, F-Layered-3, and F-Layered-4—which yield values between 3.64×10^{-4} and 4.32×10^{-4} . Taking the mean of the full-range results, we adopt a representative D/H ratio of 3.98×10^{-4} , with an estimated uncertainty of $\pm 0.34 \times 10^{-4}$, reflecting the spread among physically plausible configurations. The uncertainties reported in Table 2 are nominal 1σ statistical errors from the MCMC fits. For the full-range models, the true uncertainties are likely up to an order of magnitude larger due to underestimated observational errors and other unmodeled sources of variance. The adopted uncertainty, based on the spread among the full-range results, is therefore a conservative estimate and consistent with the broader credible intervals obtained from the error-inflated fits. Our representative D/H value is higher

than, but consistent within 2σ of, the $(2.9 \pm 0.6) \times 10^{-4}$ ratio recently reported by W. M. Grundy et al. (2024a) from analysis of a subset of the same dataset.

3.3. Preferred Model Configuration

Among the viable solutions, model F-Areal-3 yields the lowest χ_r^2 . When evaluating the Bayesian information criterion (BIC) using the inflated errors, F-Areal-3 remains the statistically favored model, with a BIC of -12578.3 compared to -12549.4 for F-Layered-3 and -12543.9 for F-Layered-4. The differences ($\Delta\text{BIC} \gtrsim 28$) represent a strong statistical preference for F-Areal-3.

Despite this, we adopt F-Layered-4 as our preferred physical configuration. While its visual agreement with the observed spectrum is close to that of F-Areal-3 and F-Layered-3, F-Layered-4 better captures the narrow 4.24- μm feature attributed to C_2H_6 —a localized band that, while contributing little to the overall

χ_r^2 , carries diagnostic importance. This configuration is also more physically motivated, reflecting the expectation that C_2H_2 and C_2H_6 form in the uppermost layers through irradiation of surface CH_4 , as previously discussed. Taken together, these considerations favor F-Layered-4 as a representative solution that balances spectral fidelity with physical plausibility. The full spectral fit for F-Layered-4 is shown in Figure 3, while a direct comparison with model F-Areal-3 is presented in Figure 6.

While the overall spectral fit is satisfactory, localized mismatches remain—most notably between 3.3 and 3.5 μm , where several C_2H_6 absorption bands occur. This may point to additional vertical or compositional complexity, such as an even thinner or more optically suppressive surface coating, that is not captured by the current model. Another clear mismatch occurs near 4.1 μm , where no satisfactory candidate has been identified, including SO_2 (W. M. Grundy et al. 2024b). Although C_2H_6 shows an absorption feature in this region, it is too weak, and the CH_3OH feature is offset toward shorter wavelengths relative to the observed one.

In our preferred configuration, the upper layer is a thin veneer with an optical thickness of ~ 0.02 , composed of an aggregate of C_2H_2 and C_2H_6 with a path length of 120 μm and a C_2H_2 volume fraction of 0.8% within the aggregate (see Appendix B). This tenuous layer likely represents a radiation-processed surface coating. Beneath it lies a lower layer dominated by two $\text{CH}_4 + \text{CH}_3\text{D}$ components with distinct path lengths (11,000 and 1,260 μm) and volume fractions (97.85% and 2.12%, respectively). The model also includes an aggregate of CH_3OH and C_2H_6 in the lower layer, characterized by a path length of 17 μm , a total volume fraction of 0.03%, and a CH_3OH content of 88.7% by volume. The retrieved D/H ratio is 3.64×10^{-4} , and the best-fit Henyey–Greenstein asymmetry parameter is $\xi = 0.23$. The MCMC posterior distributions for this model confirm that all parameters are well constrained and largely uncorrelated (Figure 8).

4. GAS-PHASE CH_4 EMISSION

Although these observations were not specifically designed in terms of resolving power or signal-to-noise ratio to investigate narrow gas-phase emission features, we report the detection of multiple emission peaks in Makemake’s spectrum near 3.3 μm , which we attribute to gas-phase CH_4 , specifically the ν_3 vibrational band and its associated P-, Q-, and R-branch structure. The observed band morphology is consistent with CH_4 fluorescence features previously identified in Chiron’s spectrum using the same spectral configuration (G395M; N.

Pinilla-Alonso et al. 2024) and subsequently confirmed with higher-resolution spectroscopy ($R \sim 2700$; I. Wong et al. 2024a; see Figure 5, panel (a)).

To isolate the CH_4 emission features, we performed a continuum subtraction using a custom spline-fitting routine. The continuum was modeled over the interval 3.254–3.390 μm , excluding regions likely affected by emission. These emission regions were identified using a CH_4 coma model that reproduces the intensity of the observed peak at 3.313 μm . All wavelengths where the model flux exceeds 3.8% of the peak value were excluded from the fit, without assuming the presence or identity of specific lines. Importantly, the remaining (unmasked) intervals closely follow the visually apparent continuum in the observed spectrum. The resulting continuum fit (magenta line in Figure 5a) was subtracted from the original flux-calibrated spectrum to produce the continuum-removed data shown in Figure 5(b) and (c).

Although some points in the spectrum exhibit large uncertainties, several features are consistent with statistically significant emission. For example, the data point at 3.313 μm has a flux of 1.360 μJy and a 1σ uncertainty of 0.124 μJy , corresponding to an $\sim 11\sigma$ detection above the local continuum. These uncertainties incorporate both measurement error and dither-to-dither scatter, with the latter being the dominant source of uncertainty (see Appendix A).

We considered two plausible origins for the CH_4 emission: (1) gas release resulting from surface sublimation, as on a comet, or from cryovolcanic activity producing plume-like emissions from the interior and (2) a thin, gravitationally bound atmosphere.

To explore the first scenario, we used the Planetary Spectrum Generator (PSG) in its expanding coma mode to simulate CH_4 fluorescence emission under non-local thermodynamic equilibrium (non-LTE) conditions (G. L. Villanueva et al. 2018, and references therein). We solved for the CH_4 production rate and the rovibrational excitation temperature, which characterizes the population distribution among the molecule’s rotational and vibrational energy levels and does not correspond to the gas kinetic temperature.

The retrieved CH_4 production rate is highly sensitive to the assumed gas expansion velocity, which remains unknown for Makemake and depends on the underlying outgassing mechanism. While Makemake is unlikely to sustain a large-scale coma, the expanding coma model serves as a limiting case to estimate plausible CH_4 production rates under the assumption of free molecular escape, as might occur during transient outgassing events such as plumes. To bracket plausible regimes, we con-

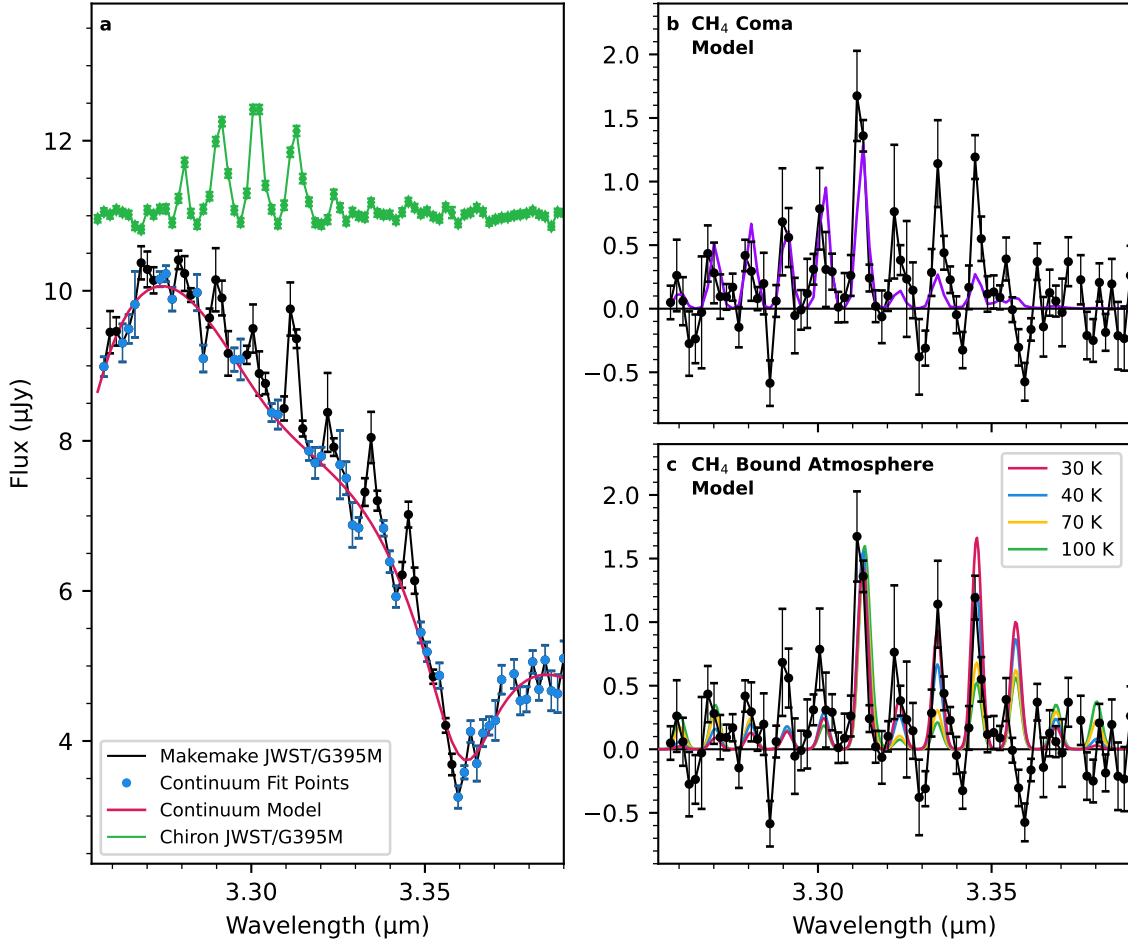


Figure 5. CH₄ gas emission in Makemake’s spectrum. (a) Observed spectrum (black) with continuum fit (magenta). Data points adopted for the continuum modeling are shown in blue (see text for details). The continuum-subtracted spectrum of Chiron, processed using a similar method, is shown for comparison (green, offset). (b) Continuum-subtracted spectrum of Makemake (black) with the best-fit CH₄ coma model overlaid (purple). (c) Same spectrum as in (b), compared to fluorescence models for a bound CH₄ atmosphere at 30, 40, 70, and 100 K (magenta, blue, yellow, and green, respectively).

sidered a range of physically motivated velocities. At the upper end, we adopted $\sim 700 \text{ m s}^{-1}$, corresponding to Makemake’s escape velocity based on a radius of 715 km and an assumed bulk density of 1.7 g cm^{-3} . Comparable expansion velocities have been observed on Ceres, where localized sources of water vapor reach $300\text{--}700 \text{ m s}^{-1}$ —consistent with Ceres’s escape velocity of $\sim 520 \text{ m s}^{-1}$ and attributed to sublimation or cryovolcanism (M. Küppers et al. 2014). On Enceladus, water plumes expand at 540 m s^{-1} —more than twice its escape velocity of $\sim 240 \text{ m s}^{-1}$ —likely due to localized pressurization (G. L. Villanueva et al. 2023).

To simulate comet-like sublimation, we adopted the empirical scaling law from N. Biver et al. (2002), originally developed to reproduce CO line profiles in comet Hale–Bopp, yielding 320 m s^{-1} . A similar velocity, on the order of 400 m s^{-1} , has been reported for comet

C/2014 UN₂₇₁ at 17 AU, supporting the plausibility of such values even under low solar insolation (N. X. Roth et al. 2025). Alternatively, the A. H. Delsemme (1982) scaling law yields 110 m s^{-1} , offering a conservative estimate for thermally driven outflow. We therefore adopt $100\text{--}700 \text{ m s}^{-1}$ as a physically plausible range for the CH₄ expansion velocity.

As expected, the retrieved production rate increases with increasing velocity. At 100 m s^{-1} , we obtained a CH₄ production rate of $(2.26 \pm 0.27) \times 10^{27} \text{ molecules s}^{-1}$ and a rovibrational excitation temperature of $34.6 \pm 6.5 \text{ K}$. At 700 m s^{-1} , the production rate increases to $(1.57 \pm 0.18) \times 10^{28} \text{ molecules s}^{-1}$, with a similar excitation temperature of $34.9 \pm 6.7 \text{ K}$.

The PSG coma model yields a reduced chi-squared value of 2.5, indicating an acceptable fit. While the model reproduces the observed $3.313\text{-}\mu\text{m}$ emission

peak—associated with the Q-branch of the CH_4 ν_3 vibrational mode—and captures shorter—wavelength R-branch features, it does not adequately match the longer-wavelength P-branch emission (see Figure 5(b)). This discrepancy highlights limitations in the model’s ability to fully reproduce the observed band structure across the entire ν_3 manifold. Notably, other volatiles such as CH_3OH and C_2H_6 exhibit emission features near the CH_4 P-branch and may contribute to the observed profile, though their involvement would imply sublimation temperatures above 40 K.

We also considered the possibility that the CH_4 emission originates from a bound atmosphere on Makemake. For this initial analysis, rather than developing fully self-consistent non-LTE excitation models, we adopted a semiempirical approach similar to that used by E. Lellouch et al. (2025) for modeling CH_4 fluorescence at 7.7 μm (ν_4 band) on Pluto. In that work, vibrational temperature (T_{vib}) profiles were incorporated into an otherwise LTE radiative transfer framework and adjusted to match the observed spectra.

However, our approach differs from that of E. Lellouch et al. (2025) in two respects. First, we followed the formalism of D. P. Edwards et al. (1993) to implement the $T_{\text{vib}}(z)$ profiles, specifically using their equations (9)–(11), (14), and (19). Second, unlike in the Pluto case—where independent constraints on the atmospheric structure (e.g., pressure, temperature, and CH_4 abundance profiles) enabled the retrieval of $T_{\text{vib}}(z)$ from the data—no such constraints exist for Makemake. The only available constraint is an upper limit on the surface pressure of 4–12 nbar from stellar occultation results (J. L. Ortiz et al. 2012).

Assuming a pure CH_4 , hydrostatic, and isothermal atmosphere, we specified $T_{\text{vib}}(z)$ profiles and adjusted the surface pressure to approximately reproduce the observed flux levels in the ν_3 band, particularly the peak flux of 1.360 μJy at 3.313 μm . For this purpose, we fixed $T_{\text{vib}} = 220$ K at all altitudes—a value close to the expected fluorescence equilibrium temperature at Makemake’s heliocentric distance of 52.65 AU. Given the low pressures involved (1–10 nbar, comparable to the 360–500 km altitude range in Pluto’s atmosphere), assuming an isothermal $T_{\text{vib}}(z)$ profile is justified.

We explored four representative gas kinetic temperatures ($T_{\text{kin}} = 30, 40, 70$, and 100 K). The first two cases correspond to an atmosphere in thermal equilibrium with the surface, while 70 K and 100 K are characteristic of Pluto’s upper atmosphere and stratopause, respectively. The corresponding inferred surface pressures required to match the observed ν_3 flux are approximately 20, 10, 2.5, and 1 pbar, respectively.

Although the fits are not perfect (see Figure 5c), they reproduce the overall band shape reasonably well. The R-branch (shortward of 3.31 μm) is systematically underestimated in all cases, while the structure in the P-branch up to 3.35 μm is best matched by the $T_{\text{kin}} = 40$ K model. While more sophisticated non-LTE modeling—such as that developed for Titan’s atmosphere (M. García-Comas et al. 2011)—is ultimately needed, the 40 K model yields the best overall match among the scenarios explored. The surface pressure required to match the observed flux in this case is about 10 pbar, well below the upper limit from J. L. Ortiz et al. (2012). At this pressure, the sublimation equilibrium temperature of pure CH_4 ice is 32.6 K (N. Fray & B. Schmitt 2009), consistent with surface temperatures for Makemake (Appendix D). This supports the scenario of a tenuous, gravitationally bound CH_4 atmosphere sustained by surface sublimation.

5. DISCUSSION AND CONCLUSIONS

We report the first detection of gas emission from Makemake, making it the third object—after Pluto and Triton—to exhibit volatile release among bodies traditionally associated with the trans-Neptunian region. The observed emission, identified as gas-phase CH_4 fluorescence near 3.3 μm , reveals a previously unrecognized expression of Makemake’s volatile inventory, likely driven by direct sublimation of CH_4 ice. While Triton is often excluded from the dynamical definition of TNOs due to its current status as a satellite of Neptune (B. Gladman et al. 2008), its likely origin as a captured body from the trans-Neptunian region (C. B. Agnor & D. P. Hamilton 2006; R. Gomes & A. Morbidelli 2024) motivates its inclusion here in a compositional context. Our results also raise the possibility that similar volatile emission may occur on other large, distant bodies, such as Eris (J. D. Hofgartner et al. 2019).

Our modeling cannot distinguish between a bound atmosphere and an expanding coma—whether isotropic or localized, as in a plume—as both scenarios reproduce the observed CH_4 emission comparably well, albeit with limitations. This ambiguity likely reflects the limited spectral resolution and signal-to-noise of the observations, which were not optimized to characterize narrow, weak fluorescence features.

The atmospheric scenario fits the data under plausible conditions, with the best match obtained for a kinetic temperature of $T_{\text{kin}} = 40$ K and a surface pressure of ~ 10 pbar. This pressure lies well below the upper limits set by occultation measurements (J. L. Ortiz et al. 2012) and is consistent with CH_4 sublimation equilibrium at Makemake’s surface temperatures.

The coma model yields CH_4 production rates of $(0.2\text{--}1.6) \times 10^{28}$ molecules s^{-1} . Assuming direct sublimation of surface CH_4 ice into vacuum, we converted these values into an effective production area (e.g., M. K. Wallis & A. K. MacPherson 1981). Using the CH_4 vapor pressure from N. Fray & B. Schmitt (2009) and an equilibrium surface temperature of ~ 30 K for Makemake, the inferred production rates correspond to localized outgassing from a region covering approximately 4–30% of the surface. This estimate is temperature-dependent; higher surface temperatures would imply smaller active areas, as the sublimation rate increases steeply with temperature.

No extended CH_4 emission is detected in the JWST data. This assessment is based on a comparison between Makemake’s radial profile in a CH_4 -integrated band map and that of a point source. However, given the spatial resolution at Makemake’s distance—approximately 3800 km per pixel—even compact coma-like features would remain unresolved, so their absence cannot be taken as evidence against coma outgassing.

One speculative explanation for the 4–30% active region is the presence of a localized hot spot driving the CH_4 emission. A similar scenario has been proposed to explain Makemake’s mid-infrared excess (C. Kiss et al. 2024), though that feature was attributed to a much smaller region (radius ~ 10 km, or $\sim 0.02\%$ of the disk) emitting at 147 ± 5 K. If such a warm region exists, it could also release less volatile species such as C_2H_6 . Given the spectral resolution and signal-to-noise of our data, we cannot rule out a contribution from C_2H_6 fluorescence. If confirmed, its presence would provide indirect support for the hot-spot hypothesis.

Assuming continuous CH_4 loss at the average production rate of 1.0×10^{28} molecules s^{-1} (~ 266 kg s^{-1}) over 4.55 Gyr, the total mass lost would amount to only $\sim 1.5\%$ of Makemake’s mass (assuming a bulk density of 1.7 g cm^{-3}). Since Makemake is currently near aphelion, this measured production rate is almost certainly a conservative lower limit to the orbit-averaged CH_4 escape flux. For context, Enceladus sustains H_2O plume activity at ~ 300 kg s^{-1} (G. L. Villanueva et al. 2023), and Ceres releases water vapor at ~ 6 kg s^{-1} (M. Küppers et al. 2014).

The D/H ratio in CH_4 ice has previously been proposed as indirect evidence for surface renewal or activity on Makemake (C. R. Glein et al. 2024; W. M. Grundy et al. 2024a). From our analysis of full-wavelength-range models, we derive a representative D/H ratio of $(3.98 \pm 0.34) \times 10^{-4}$, compared to $(2.9 \pm 0.6) \times 10^{-4}$ reported by W. M. Grundy et al. (2024a). While our value is higher, the two estimates are consistent within

2σ . Both estimates exceed the protosolar D/H in H_2 and are more in line with values measured in cometary water, though still significantly lower than the D/H in CH_4 in comet 67P (D. R. Müller et al. 2022, $(2.41 \pm 0.29) \times 10^{-3}$). Our detection of present-day outgassing or sublimation/condensation cycles raises the possibility that some postaccretion modification of the D/H ratio has occurred.

In addition to gas-phase CH_4 , our spectral modeling reveals a chemically diverse surface. The best-fit model requires a mixture of CH_4 and CH_3D , with possible CH_3OH , overlaid by aggregates of C_2H_2 and C_2H_6 —confirming earlier hydrocarbon identifications on Makemake (M. E. Brown et al. 2007). This configuration is chemically consistent with laboratory studies showing that CH_4 irradiation at cryogenic temperatures initiates C–H bond cleavage, forming CH_3 radicals that recombine to produce C_2H_6 . Continued processing can lead to irradiation products such as C_2H_4 and C_2H_2 (C. J. Bennett et al. 2006).

CH_3OH may form through recombination of CH_3 with OH radicals (with OH possibly produced from H_2O radiolysis; D. Qasim et al. 2018), via oxygen atom insertion into CH_4 ice (J. B. Bergner et al. 2017), or through radiolysis of mixed CH_4 and H_2O ices (M. H. Moore & R. L. Hudson 1998; A. Wada et al. 2006). On Makemake, solar UV photons, cosmic rays, and solar wind particles provide the energy required to drive these reactions. The low inferred abundance of CH_3OH may reflect limited access to oxygen-bearing compounds—possibly because water and other oxidants are confined to subsurface layers and are not readily available at the surface. The detection of CH_4 in the gas phase—alongside the nondetection of N_2 ice (W. M. Grundy et al. 2024a)—offers further insight into Makemake’s volatile evolution. Thermophysical models place the dwarf planet near the boundary where CH_4 and N_2 are expected to be retained (Appendix D). One possibility is that outgassed CH_4 cycles through a tenuously bound atmosphere and recondenses onto the surface—similar to the seasonal volatile transport observed on Pluto (e.g., L. A. Young 2013; G. R. Gladstone et al. 2016)—potentially masking residual N_2 beneath.

In summary, the combination of CH_4 emission, complex solid-state chemistry, and D/H ratio in CH_4 ice suggests that Makemake is not a quiescent remnant of the outer Solar System, but rather a body undergoing active or recent volatile evolution. These findings underscore the importance of continued observations of Makemake and other TNOs to probe the diversity and dynamism of distant icy worlds.

ACKNOWLEDGMENTS

This work is based on observations made with the NASA/ESA/CSA James Webb Space Telescope. The JWST data presented in this Letter were obtained from the Mikulski Archive for Space Telescopes at the Space Telescope Science Institute, which is operated by the Association of Universities for Research in Astronomy, Inc., under NASA contract NAS 5-03127 for JWST. The specific observations analyzed can be accessed via [doi: 10.17909/ac7z-9060](https://doi.org/10.17909/ac7z-9060). S.P. acknowledges Anne Verbiscer for helpful discussions on the selection of Hapke parameters, Michael S. P. Kelley for insight into expansion velocities in cometary comae, and David Nesvorny for pointing to critical literature on trans-Neptunian objects. S.P. also thanks NASA grant 80NSSC19K0402 for partial funding that supported her work. We also acknowledge the SSHADE database, the Cosmic Ice Laboratory, and the optical constants database maintained by William M. Grundy at <http://www2.lowell.edu/users/grundy/ice.html> for providing open-access optical constants essential to this work. E.L., R.B., and A.G.-L. gratefully acknowledge support from CNES (France) as part of their contributions to the JWST mission. C.K. acknowledges funding from the National Research, Development and Innovation Office (NK-FIH, Hungary) through grants K-138962 and TKP2021-NKTA-64. P.S.-S. acknowledges financial support from the Spanish I+D+i project PID2022-139555NB-I00 and from the Severo Ochoa grant CEX2021-001131-S funded by MCIN/AEI/10.13039/501100011033. N.P.-A. acknowledges funding through the ATRAE program of the Ministry of Science, Innovation, and Universities and the State Agency for Research in Spain.

AUTHOR CONTRIBUTIONS

S.P. oversaw all aspects of the project. B.J.H., A.H.P., S.N.M., and H.B.H. designed and coordinated the JWST observations. S.P. and I.W. independently reduced the JWST data to validate the spectral extraction of both solid-state and gas fluorescence features. S.P. led the modeling of the solid-state features and contributed to the analysis of gas emission and continuum modeling. I.W. led the fluorescence modeling using a coma model with PSG, while E.L. led the fluorescence modeling assuming a gravitationally bound atmosphere. P.E.J. led the analysis of volatile loss and retention with T.M. providing inputs on physical parameters of TNOs. W.M.G. and C.R.G. provided feedback on the D/H ratio computation, and J.P.E. and R.B. contributed input on the C_2H_6 optical constants. I.W., E.L., P.E.J., C.R.G., T.M., R.B., B.J.H., A.G.-L., and P.S.-S. provided critical feedback on the manuscript.

Facilities: JWST

Software: NumPy (C. R. Harris et al. 2020), Matplotlib (J. D. Hunter 2007), SciPy (P. Virtanen et al. 2020), Astropy (Astropy Collaboration et al. 2013, 2018, 2022), Photutils (L. Bradley et al. 2024), emcee (D. Foreman-Mackey et al. 2013), SBPy (M. Mommert et al. 2019), Planetary Spectrum Generator (G. L. Villanueva et al. 2018)

APPENDIX

A. OBSERVATIONS, DATA REDUCTION, AND SPECTRAL EXTRACTION

The JWST/NIRSpec observations of Makemake were obtained using three medium-resolution grating/filter combinations: G140M/F100LP, G235M/F170LP, and G395M/F290LP. For each spectral setting, pairs of dithered exposures were acquired using the 2-POINT-NOD pattern, with dither positions separated by approximately $2.3''$. The NRSIFU2RAPID readout mode was selected to reduce the level of read noise on the detectors. The effective exposure times were 292 s for G140M/F100LP, 875 s for G235M/F170LP, and 1,751 s for G395M/F290LP, yielding a total integration time of 2,918 s. Details of the observations are summarized in Table 1.

Our reduction of the JWST data closely followed the methodology described by S. Protopapa et al. (2024). The uncalibrated data were retrieved from the Mikulski Archive for Space Telescopes and processed locally using Stages 1 and 2 of the JWST calibration pipeline (Version 1.17.0; H. Bushouse et al. 2024), resulting in flat-fielded, distortion-corrected, wavelength- and flux-calibrated data cubes expressed in units of $MJy\ sr^{-1}$. Reference files were automatically drawn from context `jwst_1321.pmap` of the JWST Calibration Reference Data System. Unlike in previous work, we did not manually correct the residual correlated detector read noise (so-called 1/f noise). Instead, the 1/f noise was corrected using the NSClean algorithm included in Stage 2 of the calibration pipeline (see B. J. Rauscher 2024).

The centroid of Makemake within the field of view was determined from median-averaged images computed over wavelength ranges where the target PSF was clearly visible, after masking pixels with nonzero data quality flags. Centroid positions were measured by fitting a two-dimensional Gaussian model to the target PSF.

To identify outliers in the background region, we first masked the 7×7 pixel spectral extraction region centered on the target in each wavelength slice (solid gold box in Figure 1a–b). We then applied two-dimensional sigma clipping with an 8σ threshold, using the mean and standard deviation of the unmasked pixels as reference statistics. This step removed outliers from the background while preserving Makemake’s PSF. No additional filtering was applied along the wavelength axis at the pixel level.

After masking outliers, we performed background subtraction on a slice-by-slice basis. At each wavelength, the median background level was computed using only the pixels outside an 11×11 pixel box centered on the target (dashed gold box in panels a and b of Figure 1), and this value was subtracted from the entire image slice. The uncertainty on the background estimate was propagated in quadrature into the pixel flux uncertainties.

Spectra were then extracted from the background-subtracted cubes using a 7×7 pixel box centered on the target as the extraction aperture (solid gold box in panels a and b of Figure 1). Three independent methods were implemented: (1) Standard aperture photometry, performed by summing the flux within the extraction aperture and propagating the associated uncertainties in quadrature. (2) Manual PSF fitting, in which a local PSF template was constructed at each wavelength by computing the two-dimensional median of all images within a ± 10 slice window. Pixels outside the 7×7 extraction aperture were set to zero, and the template was normalized to a unit sum. The PSF was then scaled to the data using an error-weighted least-squares minimization, with a single multiplicative factor as the free parameter. Analogous methods have been applied to numerous NIRSpec solar system observations in the published literature (e.g., [I. Wong et al. 2024b](#)). (3) Basic PSF-based photometric extraction using the `BasicPSFPhotometry` routine in `astropy`, with the same fixed centroid and two-dimensional PSF model as in method 2.

After multiplying by the nominal pixel area in steradians, each method produced a flux-calibrated spectrum (in MJy) with associated uncertainties. The resulting spectra were optionally cleaned to remove outlier data points using a combination of relative error filtering and

a rolling sigma filter. All three approaches were implemented to ensure confidence in the final extracted spectrum. Methods 2 and 3 yielded very similar results, confirming the mutual consistency of the PSF-based techniques. Both PSF-based methods closely matched the aperture photometry in absolute flux and spectral shape, but provided superior signal-to-noise ratios across the full spectral range. For the analysis in this Letter, we adopted the spectrum extracted using basic PSF photometry (method 3), after filtering away points with relative errors that exceeded the mean value by 20σ .

To improve the precision of the spectrum within each grating, we averaged the spectra obtained from the two dither positions. Uncertainties were estimated by propagating the individual errors and incorporating the scatter between dithers through a quadrature sum. We masked wavelengths in the averaged spectrum where the relative error exceeded a threshold defined as the mean plus 5σ , based on sigma-clipped statistics computed from the distribution of relative errors across the full spectrum. The resulting filtered mean spectrum was used for subsequent analysis.

To correct for flux losses outside of the aperture and recover the total flux of the target, we used NIRSpec observations of the G2V-type solar analog star GSPC P330-E, obtained as part of the Cycle 2 flux calibration program #04498. The star’s spectrum was extracted using the same methodology and 7×7 pixel aperture as was applied to Makemake. By dividing the extracted stellar spectrum by the CALSPEC model spectrum of P330-E ([R. C. Bohlin et al. 2014](#)), convolved to match the resolving power of the NIRSpec filters supplied by the JWST user documentation, we derived a wavelength-dependent correction factor that quantified the fraction of the total flux captured within the extraction aperture. This correction array was then applied to the extracted Makemake spectrum to obtain an unbiased flux estimate. Contrary to [S. Protopapa et al. \(2024\)](#), no smoothing was applied to the correction array.

The final step was the conversion of the flux-calibrated spectrum to reflectance (I/F), following the procedure described by [S. Protopapa et al. \(2024\)](#). The calculation used a heliocentric distance of 52.653 AU, a target–observer distance of 52.209 AU, and Makemake’s measured diameter of 1,430 km ([J. L. Ortiz et al. 2012](#)).

B. SPECTRAL MODELING

The modeling algorithm adopted in this work is based on the Hapke radiative transfer theory ([B. Hapke 1993, 2002, 2012](#)). Our specific implementation follows the framework outlined in [S. Protopapa et al. \(2017, 2020\)](#), in which the formulation of the radiance factor (I/F)

Table 1. Details of the JWST/NIRSpec Observations (Program #1254)

File Name	Start Time (UTC)	Grating	Filter	Exp. Time (s)
jw01254004001.02101.00001	2023 Jan 29 23:34:32.591	G140M	F100LP	145.889
jw01254004001.02101.00002	2023 Jan 29 23:40:22.735	G140M	F100LP	145.889
jw01254004001.02103.00001	2023 Jan 29 23:48:24.208	G235M	F170LP	437.667
jw01254004001.02103.00002	2023 Jan 29 23:59:20.719	G235M	F170LP	437.667
jw01254004001.02105.00001	2023 Jan 30 00:12:13.928	G395M	F290LP	875.333
jw01254004001.02105.00002	2023 Jan 30 00:30:13.543	G395M	F290LP	875.333

accounts for multiple scattering, the shadow-hiding opposition effect, and macroscopic surface roughness. We explored a range of physically motivated surface configurations, including intimate mixtures, areal mixtures, and stratified (layered) geometries.

Consistent with [W. M. Grundy et al. \(2024a\)](#), we assumed that only the single-scattering albedo w varies with wavelength. The remaining Hapke photometric parameters were fixed to the values derived by [A. J. Verbiscer et al. \(2022\)](#) for Makemake: a shadow-hiding opposition effect amplitude and width of $B_0 = 1.0$ and $h = 0.11$, respectively, and a macroscopic roughness angle of $\theta = 5^\circ$. The cosine asymmetry parameter ξ , which characterizes the angular distribution of scattered light, was treated as a free parameter. This choice reflects the differences between the near-infrared wavelengths probed by JWST and the visible-wavelength observations (607.6 nm) used by [A. J. Verbiscer et al. \(2022\)](#). Previous work on Charon has shown that photometric parameters can vary with wavelength due to changes in scattering regime and penetration depth ([S. Protopapa et al. 2020](#)). Of the Hapke parameters, ξ exerts the strongest influence on the near-infrared continuum, particularly in regions of saturated absorption near 3 μm . Allowing ξ to vary provides the flexibility needed to reproduce the spectral behavior across the full wavelength range while minimizing the number of free parameters.

The remaining free parameters in the model include the optical path length (D , a proxy for grain size); the abundance of each compound, expressed as either fractional area (F) in areal mixtures or fractional volume (V) in intimate mixtures; the D/H ratio; and, in the case of aggregates, the relative volume fractions of the individual components. For stratified geometries, an additional free parameter is the optical thickness of the top layer (τ).

For the aggregates, we estimated the real and imaginary parts of the refractive index as a function of wavelength (λ) using effective medium theory—specifically,

the Bruggeman mixing formula ([C. F. Bohren & D. R. Huffman 1983](#)). This approach preserves the spectral properties of each component within the aggregate and assumes that the end-members remain distinct from one another at the molecular level. By applying this formalism, we obtained effective optical constants that reflect the spectral behavior of the composite material, which were then used as input to the Hapke model.

To determine the best-fit values of these free parameters, we first performed Levenberg–Marquardt (LM) optimization to obtain an initial solution. This preliminary fit was then used to initialize an MCMC analysis, which was employed to explore the posterior distributions and quantify parameter uncertainties. Convergence was assessed using the autocorrelation time and visual inspection of the chains to ensure they were well mixed and stationary. After confirming convergence, we performed a final LM optimization, initialized with the median values from the MCMC chains, to refine the solution and improve the residuals. This hybrid approach combines the computational efficiency of deterministic fitting with the statistical rigor of probabilistic sampling.

Modeling the JWST spectrum requires optical constants for each compound in the mixture that are consistent with both the spectral coverage of the data and the temperature conditions relevant to Makemake’s surface. The following section ([Appendix C](#)) outlines the methods used to derive deuterium-free optical constants for CH_4 ice and describes the optical constants adopted for C_2H_6 . Optical constants for other compounds were sourced directly from the literature and databases cited in the main text ([Section 3](#)).

We systematically explored the effects of wavelength coverage, mixing geometry, and compositional complexity on both the derived D/H ratio and the overall quality of the spectral fit. [Table 2](#) summarizes the full suite of models tested in this study. Model names encode the wavelength range (S = short: 2.0–2.7 μm , M = medium: 2.7–4.2 μm , L = long: 4.1–4.8 μm , F = full:

2.0–4.8 μm), surface mixing geometry (Intimate, Areal, or Layered), and compositional complexity: 1 = ($\text{CH}_4 + \text{CH}_3\text{D}$) only; 2 = 1 + ($\text{C}_2\text{H}_2 + \text{C}_2\text{H}_6$); 3 = 2 + CH_3OH ; 4 = 2 + ($\text{CH}_3\text{OH} + \text{C}_2\text{H}_6$). All models include two components of ($\text{CH}_4 + \text{CH}_3\text{D}$). The table lists the reduced chi-squared values (χ_r^2) and D/H ratios, where constrained.

Figure 6 compares the best-fit synthetic spectra from models F–Areal–2, F–Areal–3, and F–Layered–4. This progression illustrates the impact of increasing compositional complexity. The model F–Areal–2, which includes only $\text{CH}_4 + \text{CH}_3\text{D}$ and $\text{C}_2\text{H}_2 + \text{C}_2\text{H}_6$, fails to reproduce the observed continuum, particularly beyond 3.5 μm . To compensate for the missing flux in this region, the model artificially increases the contribution from CH_4 , resulting in absorption bands near 2.3 μm that are deeper than observed. Incorporating CH_3OH (F–Areal–3) improves the continuum fit significantly, while F–Layered–4 introduces a stratified geometry that better captures subtle features such as the narrow C_2H_6 absorption at 4.24 μm .

Although models F–Areal–3 and F–Layered–4 yield similar reduced chi-squared values, they differ in their physical assumptions, the degree of surface heterogeneity they imply, and the retrieved D/H ratios. The corresponding MCMC posterior distributions are shown in Figures 7 and 8, confirming that both models are well constrained. Notably, F–Layered–4 achieves improved spectral fidelity in key diagnostic regions, supporting its adoption as the more physically plausible configuration.

C. OPTICAL CONSTANTS

C.1. Deuterium-free methane optical constants

W. M. Grundy et al. (2002) reported temperature-dependent absorption coefficients (α) for pure CH_4 and identified CH_3D absorption features at 4.34 and 4.56 μm attributed to trace deuterium content. W. M. Grundy et al. (2011) later validated this assignment, identified additional (though weaker) CH_3D features at 2.47 and 2.87 μm , determined a $\text{CH}_3\text{D}/\text{CH}_4$ ratio of 3.3×10^{-4} for the same sample, and provided temperature-dependent absorption coefficients for CH_3D . Following Equation 1 of W. M. Grundy et al. (2011), we derived deuterium-free, temperature-dependent CH_4 absorption coefficients (α_{CH_4}) by subtracting the CH_3D contribution ($\alpha_{\text{CH}_3\text{D}}$) from the original CH_4 $\alpha_{\text{G'02}}$ values of W. M. Grundy et al. (2002).

The imaginary part of the refractive index, k , was calculated from our α_{CH_4} values at 40 K using the relation $\alpha = 4\pi k/\lambda$. These values were compared with the SSHADE/GhoSST dataset for crystalline CH_4 -I at 39 ± 1 K (F. Trotta 1996; W. M. Grundy et al. 2002), which provides both the real (n) and imaginary (k) com-

ponents of the refractive index. These were derived from laboratory transmission measurements via iterative inversion using a thin-film plus substrate optical model combined with Kramers–Kronig analysis over the spectral range 0.71–17.2 μm . For wavelengths shorter than 5 μm , k values below 10^{-2} were not directly measured but computed from the absorption coefficients of W. M. Grundy et al. (2002), assuming the small- k limit. Residual H_2O and CO_2 gas features were interpolated out.

Given the excellent agreement between our derived k values and those in the SSHADE dataset, we adopted the SSHADE n values and interpolated them onto the wavelength grid of the JWST spectrum.

To further refine the k spectrum, we adopted SSHADE k values in the 2.66–2.76 μm range, which appear less noisy—likely due to more effective removal of residual gas features during SSHADE processing. We also replaced the 3.25–3.40 μm interval, which includes the broad CH_4 absorption near 3.1 μm that is missing from W. M. Grundy et al. (2002) due to sample thickness limitations. Finally, to suppress small-amplitude numerical oscillations, we applied a smoothing spline over the 4.19–4.37 μm region.

The final optical constants were assembled by combining the interpolated n values from SSHADE with the corrected k spectrum. This synthetic (λ , n , k) dataset represents the optical properties of CH_4 ice without contamination from CH_3D at 40 K—appropriate for Make-make—and was used in our radiative transfer modeling. A comparison of the original, modified, and smoothed k spectra is shown in Figure 9.

C.2. Ethane Optical Constants

We adopted optical constants for C_2H_6 ice provided by R. Mastrapa (private communication), which consistently yielded better spectral fits to the JWST data than those from other available datasets. Comparison sources included measurements from SSHADE (15 K crystalline; F. Trotta 1996), the Cosmic Ice Laboratory (40 K crystalline and amorphous; R. L. Hudson et al. 2014b), and G. Molpeceres et al. (2016, 18 K amorphous). The Mastrapa optical constants yield better agreement with the observed depth and shape of key ethane absorption features, particularly in the 3.1–3.6 μm region. These same optical constants were also adopted in the analysis of TNO spectra by J. P. Emery et al. (2024), further supporting their relevance for modeling outer solar system surfaces.

However, this dataset also exhibits a broad absorption feature between 3.20 and 3.29 μm that partially overlaps with bands attributed to C_2H_4 . To evaluate potential contamination or spectral blending, we compared the

Table 2. Summary of spectral models explored in this study. Model names use abbreviations for the wavelength range (S = short, 2.0–2.7 μm ; M = medium, 2.7–4.2 μm ; L = long, 4.1–4.8 μm ; F = full, 2.0–4.8 μm), mixing geometry (Intimate, Areal, Layered), and compositional complexity: 1 = ($\text{CH}_4 + \text{CH}_3\text{D}$) only, 2 = 1 + ($\text{C}_2\text{H}_2 + \text{C}_2\text{H}_6$), 3 = 2 + CH_3OH , 4 = 2 + ($\text{CH}_3\text{OH} + \text{C}_2\text{H}_6$). All models include two sets of ($\text{CH}_4 + \text{CH}_3\text{D}$). Quoted D/H uncertainties should be regarded as lower limits; the true uncertainties may be up to an order of magnitude larger due to underestimated observational errors and other unmodeled sources of variance (see text for details).

Model Name	Composition Description	χ_r^2	D/H
S-Intimate-1	$2\times(\text{CH}_4 + \text{CH}_3\text{D})$ only	34.4	—
M-Intimate-1	$2\times(\text{CH}_4 + \text{CH}_3\text{D})$ only	236.5	—
L-Intimate-1	$2\times(\text{CH}_4 + \text{CH}_3\text{D})$ only	25.1	$3.62^{+0.02}_{-0.02} \times 10^{-4}$
S-Intimate-2	$2\times(\text{CH}_4 + \text{CH}_3\text{D}) + (\text{C}_2\text{H}_2 + \text{C}_2\text{H}_6)$	13.7	—
M-Intimate-2	$2\times(\text{CH}_4 + \text{CH}_3\text{D}) + (\text{C}_2\text{H}_2 + \text{C}_2\text{H}_6)$	119.8	—
L-Intimate-2	$2\times(\text{CH}_4 + \text{CH}_3\text{D}) + (\text{C}_2\text{H}_2 + \text{C}_2\text{H}_6)$	21.5	$3.54^{+0.02}_{-0.03} \times 10^{-4}$
S-Areal-2	$2\times(\text{CH}_4 + \text{CH}_3\text{D}) + (\text{C}_2\text{H}_2 + \text{C}_2\text{H}_6)$	12.0	—
M-Areal-2	$2\times(\text{CH}_4 + \text{CH}_3\text{D}) + (\text{C}_2\text{H}_2 + \text{C}_2\text{H}_6)$	118.1	—
L-Areal-2	$2\times(\text{CH}_4 + \text{CH}_3\text{D}) + (\text{C}_2\text{H}_2 + \text{C}_2\text{H}_6)$	24.5	$3.59^{+0.02}_{-0.02} \times 10^{-4}$
F-Areal-2	$2\times(\text{CH}_4 + \text{CH}_3\text{D}) + (\text{C}_2\text{H}_2 + \text{C}_2\text{H}_6)$	136.4	—
F-Intimate-2	$2\times(\text{CH}_4 + \text{CH}_3\text{D}) + (\text{C}_2\text{H}_2 + \text{C}_2\text{H}_6)$	132.1	—
F-Layered-2	$(\text{C}_2\text{H}_2 + \text{C}_2\text{H}_6)$ over $2\times(\text{CH}_4 + \text{CH}_3\text{D})$	134.4	—
F-Areal-3	$2\times(\text{CH}_4 + \text{CH}_3\text{D}) + (\text{C}_2\text{H}_2 + \text{C}_2\text{H}_6) + \text{CH}_3\text{OH}$	79.7	$4.32^{+0.02}_{-0.02} \times 10^{-4}$
F-Layered-3	$(\text{C}_2\text{H}_2 + \text{C}_2\text{H}_6)$ over $2\times(\text{CH}_4 + \text{CH}_3\text{D}) + \text{CH}_3\text{OH}$	80.9	$3.64^{+0.01}_{-0.01} \times 10^{-4}$
F-Layered-4	$(\text{C}_2\text{H}_2 + \text{C}_2\text{H}_6)$ over $2\times(\text{CH}_4 + \text{CH}_3\text{D}) + (\text{CH}_3\text{OH} + \text{C}_2\text{H}_6)$	80.8	$3.64^{+0.01}_{-0.01} \times 10^{-4}$

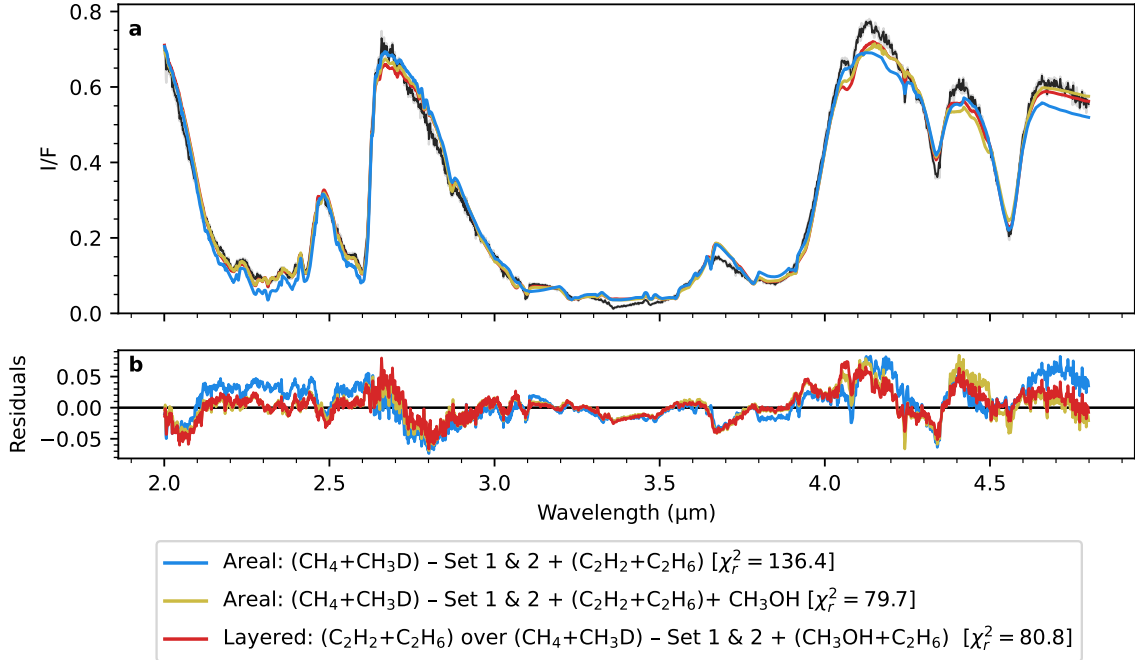


Figure 6. Illustration of the effect of compositional complexity and layering geometry. Comparison of three spectral models for Makemake over the full wavelength range (2.0–4.8 μm), overlaid on the observed JWST spectrum (black). All models include two components of ($\text{CH}_4 + \text{CH}_3\text{D}$). The blue curve corresponds to the baseline model (F-Areal-2), which includes only $\text{CH}_4 + \text{CH}_3\text{D}$ and $\text{C}_2\text{H}_2 + \text{C}_2\text{H}_6$. The muted yellow curve (F-Areal-3) adds CH_3OH to improve the continuum fit across the spectrum. The red curve represents the final model (F-Layered-4), which assumes a stratified surface where a $\text{C}_2\text{H}_2 + \text{C}_2\text{H}_6$ aggregate overlays two $\text{CH}_4 + \text{CH}_3\text{D}$ components and a $\text{CH}_3\text{OH} + \text{C}_2\text{H}_6$ aggregate, yielding the most favorable overall fit (see main text for details). Residuals for each model are shown in the lower panel.

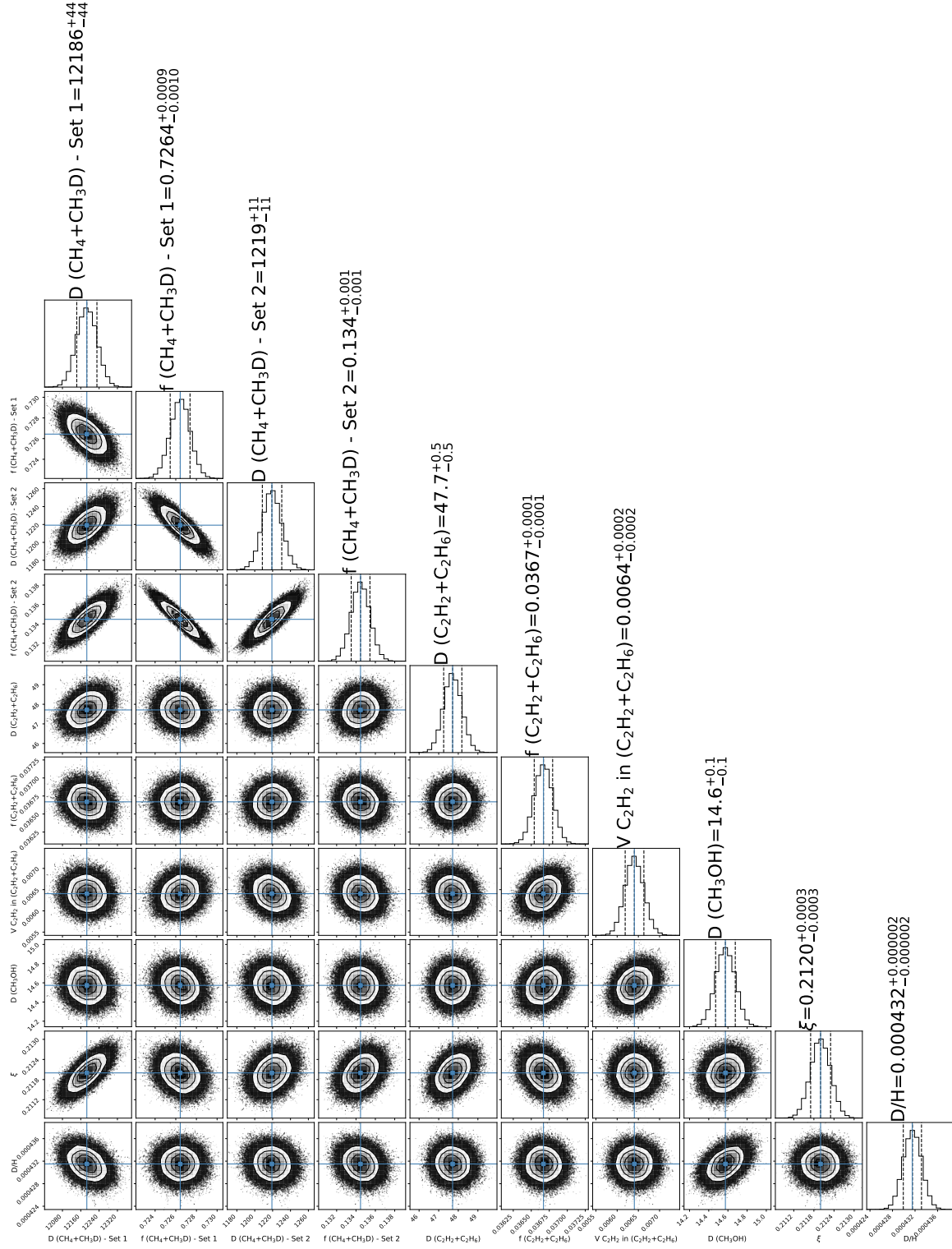


Figure 7. Posterior distributions of the free parameters in model F-Areal-3. Corner plot showing the marginalized posterior probability distributions from the MCMC fit to the JWST spectrum of Makemake. Contours in the two-dimensional histograms represent the 1σ , 2σ , and 3σ credible regions. Dashed lines in the one-dimensional histograms indicate the 16th, 50th (median), and 84th percentiles. All parameters are well constrained and largely uncorrelated, with the exception of a slight correlation between the two $\text{CH}_4 + \text{CH}_3\text{D}$ components, as expected from their overlapping spectral contributions. Solid cyan lines indicate the parameter values obtained from the second Levenberg–Marquardt optimization. All results shown correspond to the nominal fits using the original observational uncertainties. When the analysis was repeated with data uncertainties inflated by a factor of 9 (to bring χ^2_{r} of F-Areal-3 to unity), the posterior medians remained consistent, but the credible intervals widened by approximately an order of magnitude (see text for details).

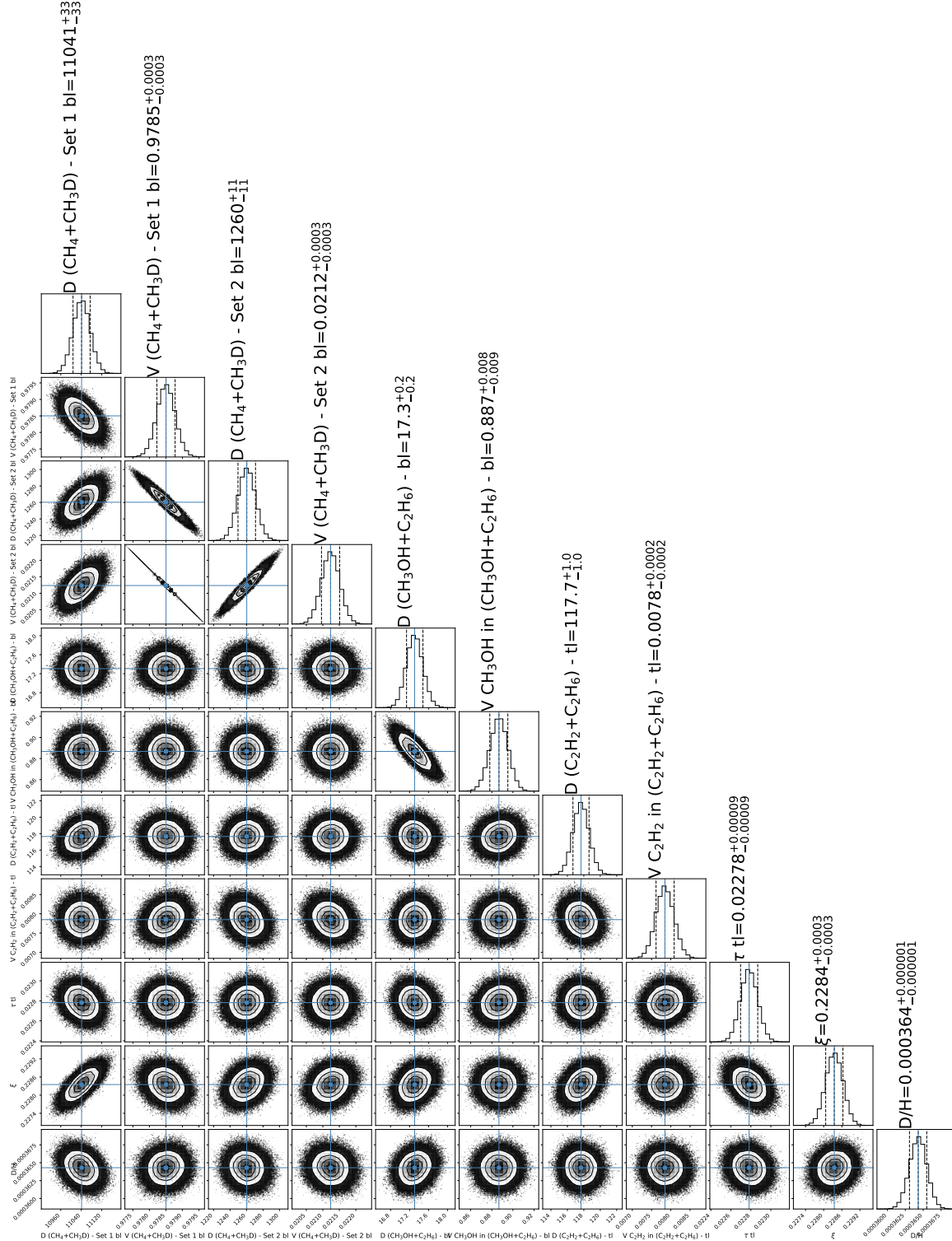


Figure 8. Posterior distributions of the free parameters in model F-Layered-4. Corner plot showing the marginalized posterior probability distributions from the MCMC fit to the JWST spectrum of Makemake. Contours in the two-dimensional histograms represent the 1σ , 2σ , and 3σ credible regions. Dashed lines in the one-dimensional histograms indicate the 16th, 50th (median), and 84th percentiles. All parameters are well constrained, although a strong correlation is observed between the two $\text{CH}_4+\text{CH}_3\text{D}$ components, as expected due to their overlapping spectral contributions. Solid cyan lines indicate the parameter values obtained from the second Levenberg-Marquardt optimization. Parameters associated with the bottom and top layers are labeled **bl** and **tl**, respectively. All results shown correspond to the nominal fits using the original observational uncertainties. When the analysis was repeated with data uncertainties inflated by a factor of 9 (to bring χ^2_r of F-Areal-3 to unity), the posterior medians remained consistent, but the credible intervals widened by approximately an order of magnitude (see text for details).

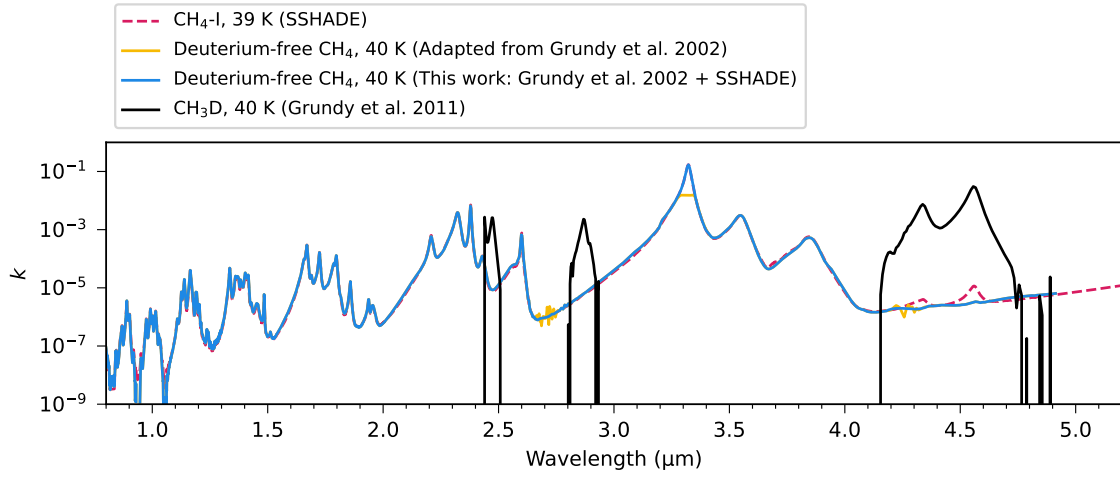


Figure 9. Comparison of the imaginary part of the refractive index (k) for CH_4 and CH_3D ices near 40 K. The black curve shows the total CH_3D contribution derived from [W. M. Grundy et al. \(2011\)](#). The magenta dashed curve corresponds to the SSHADe dataset for crystalline $\text{CH}_4\text{-I}$ at 39 K, which includes CH_3D absorption bands. The orange curve represents deuterium-free CH_4 at 40 K, derived from the absorption coefficients of [W. M. Grundy et al. \(2002\)](#) following the CH_3D subtraction procedure described in [W. M. Grundy et al. \(2011\)](#). Notably, unlike the SSHADe dataset, the orange curve does not display CH_3D absorption features. The blue curve shows the final corrected CH_4 optical constants used in this study, which combine deuterium-free k values with SSHADe-derived values in selected spectral regions.

Mastrapa dataset to the other C_2H_6 optical constants noted above, as well as to C_2H_4 data obtained at 60 K (crystalline; R. L. Hudson et al. 2014b). We found that the SSHADE and Molpeceres datasets do not exhibit significant absorption in this range, whereas both the 40 K amorphous and crystalline datasets from the Cosmic Ice Laboratory do.

The spectral profile of the 3.20–3.29 μm feature in the Mastrapa dataset differs from that of known C_2H_4 bands, though some degree of overlap cannot be ruled out. Moreover, correcting this region for possible C_2H_4 contamination would also alter the broader 3.36- μm region, where all C_2H_6 datasets—regardless of source—show an intrinsic absorption feature. While some ambiguity remains, we chose to retain the Mastrapa dataset without modification for use in our modeling. A comparison of the C_2H_6 and C_2H_4 optical constants from various sources is shown in Figure 10.

D. VOLATILE LOSS AND RETENTION

Volatile ices on the surfaces of TNOs are subject to escape processes that, without replenishment from the interior or through surface chemistry, can deplete surface reservoirs over time. Although the physics of atmospheric escape remains complex and poorly constrained—even for well-studied bodies like Pluto (e.g., D. F. Strobel 2021)—simplified models provide useful first-order insights into volatile retention across the TNO population.

In this study, we build upon the surface-bounded Jeans escape framework developed by E. L. Schaller & M. E. Brown (2007); M. E. Brown et al. (2011), which assumes that mass loss occurs directly from the surface without the mediation of a sustained atmosphere. In this approximation, the escape rate depends on the object’s mass, radius, surface temperature, and the species’ vapor pressure. We update this framework using revised measurements of TNO sizes, albedos, and vapor pressure curves from W. M. Grundy et al. (2024b) and N. Fray & B. Schmitt (2009), along with updated cometary volatile mixing ratios from M. Lippi et al. (2021).

Figure 11 shows the minimum temperatures required for a TNO to lose a given fraction of its initial volatile inventory over 4.6 Gyr, based on the surface-bounded

Jeans escape model applied at fixed temperatures. The shaded regions indicate the temperature ranges over which 1% to 100% of the initial inventory would be lost, shown for various TNO sizes and volatile species. Objects falling to the right of a given volatile’s loss curve are predicted to retain that species. We also plot each TNO’s perihelion temperature (squares) and define an “equivalent temperature” (circles) that incorporates the time spent at different heliocentric distances along an eccentric orbit.

The equivalent temperature offers a more realistic assessment of volatile loss by integrating escape rates throughout the orbit, yielding a time-averaged view of mass loss. Because T_{equiv} is lower than the perihelion temperature—especially for TNOs with high eccentricities—it can shift an object from the volatile loss regime into the retention regime. This distinction is critical for assessing volatile stability in borderline cases.

Despite updates to input parameters and vapor pressure data, our conclusions remain broadly consistent with earlier studies: only the largest and coldest TNOs can retain hypervolatile ices over Gyr timescales, while smaller and warmer bodies are expected to preserve only less volatile species. Makemake lies near the retention threshold for CH_4 and N_2 , and its volatile history depends sensitively on assumptions about its Bond albedo (the product of the geometric albedo p_V and the phase integral q_V), size, and density. If Makemake is bright—as suggested by the range of Bond albedo values reported by A. J. Verbiscer et al. (2022)—then both CH_4 and N_2 could have been retained over 4.6 Gyr, assuming Jeans escape is the dominant loss mechanism. If, instead, Makemake is darker—as indicated by the lower albedo values from J. L. Ortiz et al. (2012)—then volatile retention becomes more uncertain and depends more strongly on its bulk density.

Our observations confirm the presence of CH_4 ice on Makemake’s surface but show no evidence for N_2 . From this, we conclude that CH_4 retention is consistent with expectations from surface-bounded Jeans escape, while the absence of N_2 implies that additional loss mechanisms must have been in effect. These could include hydrodynamic escape, atmospheric loss from an altitude above the surface, or depletion resulting from a past giant impact.

REFERENCES

- Agnor, C. B., & Hamilton, D. P. 2006, *Nature*, 441, 192,
doi: [10.1038/nature04792](https://doi.org/10.1038/nature04792)
- Astropy Collaboration, Robitaille, T. P., Tollerud, E. J.,
et al. 2013, *A&A*, 558, A33,
doi: [10.1051/0004-6361/201322068](https://doi.org/10.1051/0004-6361/201322068)

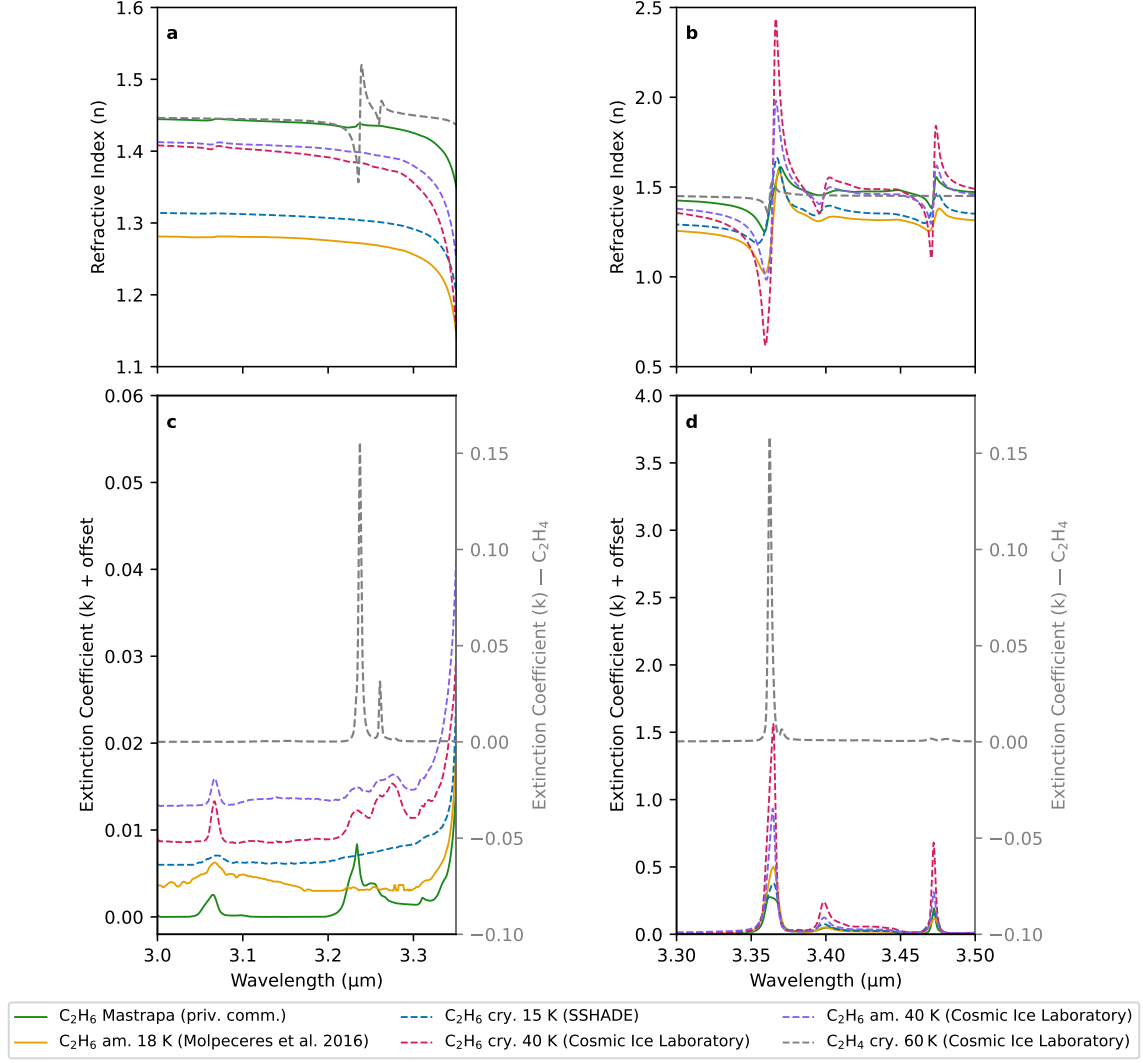


Figure 10. Comparison of C_2H_6 and C_2H_4 optical constants. Panels (a) and (c) show the refractive index (n) and extinction coefficient (k) of C_2H_6 between 3.00 and 3.35 μm , while panels (b) and (d) focus on the 3.3–3.5 μm region. Optical constants are shown for the Mastrapa dataset (private comm.), SSHADe (15 K crystalline; F. Trotta 1996), the Cosmic Ice Laboratory (40 K crystalline and amorphous; R. L. Hudson et al. 2014b), and G. Molpeceres et al. (2016, 18 K amorphous). Overlaid in gray are the optical constants of C_2H_4 at 60 K from the Cosmic Ice Laboratory database (R. L. Hudson et al. 2014b). While some overlap exists between C_2H_6 and C_2H_4 absorption bands—particularly near 3.20–3.29 μm —the Mastrapa dataset remains the most consistent with the JWST spectral features modeled in this study.

Astropy Collaboration, Price-Whelan, A. M., Sipőcz, B. M., et al. 2018, *AJ*, 156, 123, doi: [10.3847/1538-3881/aabc4f](https://doi.org/10.3847/1538-3881/aabc4f)

Astropy Collaboration, Price-Whelan, A. M., Lim, P. L., et al. 2022, *ApJ*, 935, 167, doi: [10.3847/1538-4357/ac7c74](https://doi.org/10.3847/1538-4357/ac7c74)

Bennett, C. J., Jamieson, C. S., Osamura, Y., & Kaiser, R. I. 2006, *ApJ*, 653, 792, doi: [10.1086/508561](https://doi.org/10.1086/508561)

Bergner, J. B., Öberg, K. I., & Rajappan, M. 2017, *ApJ*, 845, 29, doi: [10.3847/1538-4357/aa7d09](https://doi.org/10.3847/1538-4357/aa7d09)

Biver, N., Bockelée-Morvan, D., Colom, P., et al. 2002, *Earth Moon and Planets*, 90, 5, doi: [10.1023/A:1021599915018](https://doi.org/10.1023/A:1021599915018)

Bohlin, R. C., Gordon, K. D., & Tremblay, P. E. 2014, *PASP*, 126, 711, doi: [10.1086/677655](https://doi.org/10.1086/677655)

Bohren, C. F., & Huffman, D. R. 1983, *Absorption and scattering of light by small particles*

Böker, T., Beck, T. L., Birkmann, S. M., et al. 2023, *PASP*, 135, 038001, doi: [10.1088/1538-3873/acb846](https://doi.org/10.1088/1538-3873/acb846)

Bradley, L., Sipőcz, B., Robitaille, T., et al. 2024, 2.0.2 Zenodo, doi: [10.5281/zenodo.13989456](https://doi.org/10.5281/zenodo.13989456)

Brown, M. E. 2012, *Annual Review of Earth and Planetary Sciences*, 40, 467, doi: [10.1146/annurev-earth-042711-105352](https://doi.org/10.1146/annurev-earth-042711-105352)

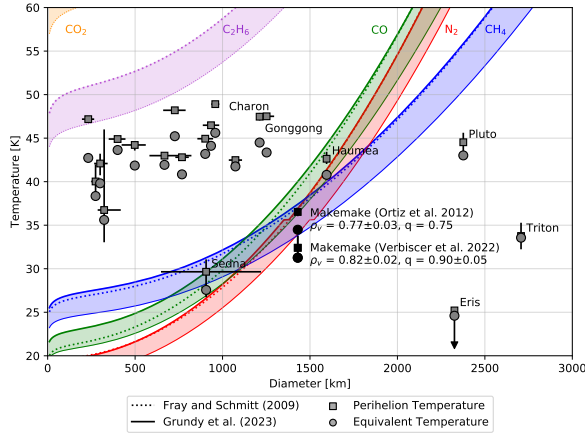


Figure 11. Perihelion (squares) and equivalent (circles) temperatures for a selection of TNOs, plotted as a function of diameter. Makemake (1430 km diameter, $p_V = 0.820 \pm 0.020$, $q = 0.90^{+0.05}_{-0.05}$ from A. J. Verbiscer et al. (2022) and $p_V = 0.77 \pm 0.03$, $q = 0.75$ from J. L. Ortiz et al. (2012)) is highlighted in black. Error bars represent uncertainties in diameter and, for perihelion temperatures, uncertainties in albedo. Colored curves indicate the threshold temperatures for volatile loss via surface-bounded Jeans escape: TNOs falling below a given curve are expected to retain that volatile species over 4.6 Gyr, while those above could have lost their entire initial inventory. Shaded regions span the temperatures required for a TNO of a given size to lose between 1% (thin line) and 100% (thick line) of its initial volatile inventory. CO_2 (yellow shaded region) is significantly less volatile than the other species, so only the 1% loss line appears within the temperature range relevant to TNOs.

Brown, M. E. 2013, *ApJL*, 767, L7, doi: [10.1088/2041-8205/767/1/L7](https://doi.org/10.1088/2041-8205/767/1/L7)

Brown, M. E., Barkume, K. M., Blake, G. A., et al. 2007, *AJ*, 133, 284, doi: [10.1086/509734](https://doi.org/10.1086/509734)

Brown, M. E., Burgasser, A. J., & Fraser, W. C. 2011, *ApJL*, 738, L26, doi: [10.1088/2041-8205/738/2/L26](https://doi.org/10.1088/2041-8205/738/2/L26)

Brown, M. E., Schaller, E. L., & Blake, G. A. 2015, *AJ*, 149, 105, doi: [10.1088/0004-6256/149/3/105](https://doi.org/10.1088/0004-6256/149/3/105)

Bushouse, H., Eisenhamer, J., Dencheva, N., et al. 2024, 1.14.0 Zenodo, doi: [10.5281/zenodo.10870758](https://doi.org/10.5281/zenodo.10870758)

Delsemme, A. H. 1982, in *IAU Colloq. 61: Comet Discoveries, Statistics, and Observational Selection*, ed. L. L. Wilkening, 85–130

Edwards, D. P., Lopez-Puertas, M., & Lopez-Valverde, M. A. 1993, *J. Geophys. Res.*, 98, 14,955, doi: [10.1029/93JD01297](https://doi.org/10.1029/93JD01297)

Emery, J. P., Wong, I., Brunetto, R., et al. 2024, *Icarus*, 414, 116017, doi: [10.1016/j.icarus.2024.116017](https://doi.org/10.1016/j.icarus.2024.116017)

Foreman-Mackey, D., Hogg, D. W., Lang, D., & Goodman, J. 2013, *PASP*, 125, 306, doi: [10.1086/670067](https://doi.org/10.1086/670067)

Fray, N., & Schmitt, B. 2009, *Planet. Space Sci.*, 57, 2053, doi: [10.1016/j.pss.2009.09.011](https://doi.org/10.1016/j.pss.2009.09.011)

García-Comas, M., López-Puertas, M., Funke, B., et al. 2011, *Icarus*, 214, 571, doi: [10.1016/j.icarus.2011.03.020](https://doi.org/10.1016/j.icarus.2011.03.020)

Gerakines, P. A., & Hudson, R. L. 2020, *ApJ*, 901, 52, doi: [10.3847/1538-4357/abad39](https://doi.org/10.3847/1538-4357/abad39)

Gladman, B., Marsden, B. G., & Vanlaerhoven, C. 2008, in *The Solar System Beyond Neptune*, ed. M. A. Barucci, H. Boehnhardt, D. P. Cruikshank, A. Morbidelli, & R. Dotson, 43–57

Gladstone, G. R., Stern, S. A., Ennico, K., et al. 2016, *Science*, 351, aad8866, doi: [10.1126/science.aad8866](https://doi.org/10.1126/science.aad8866)

Glein, C. R., Grundy, W. M., Lunine, J. I., et al. 2024, *Icarus*, 412, 115999, doi: [10.1016/j.icarus.2024.115999](https://doi.org/10.1016/j.icarus.2024.115999)

Gomes, R., & Morbidelli, A. 2024, *Icarus*, 420, 116142, doi: [10.1016/j.icarus.2024.116142](https://doi.org/10.1016/j.icarus.2024.116142)

Grundy, W. M., Morrison, S. J., Bovyn, M. J., Tegler, S. C., & Cornelison, D. M. 2011, *Icarus*, 212, 941, doi: [10.1016/j.icarus.2011.01.034](https://doi.org/10.1016/j.icarus.2011.01.034)

Grundy, W. M., Schmitt, B., & Quirico, E. 2002, *Icarus*, 155, 486, doi: [10.1006/icar.2001.6726](https://doi.org/10.1006/icar.2001.6726)

Grundy, W. M., Wong, I., Glein, C. R., et al. 2024a, *Icarus*, 411, 115923, doi: [10.1016/j.icarus.2023.115923](https://doi.org/10.1016/j.icarus.2023.115923)

Grundy, W. M., Tegler, S. C., Steckloff, J. K., et al. 2024b, *Icarus*, 410, 115767, doi: [10.1016/j.icarus.2023.115767](https://doi.org/10.1016/j.icarus.2023.115767)

Hapke, B. 1993, *Theory of reflectance and emittance spectroscopy*

Hapke, B. 2002, *Icarus*, 157, 523, doi: [10.1006/icar.2002.6853](https://doi.org/10.1006/icar.2002.6853)

Hapke, B. 2012, *Theory of Reflectance and Emittance Spectroscopy*, doi: [10.1017/CBO9781139025683](https://doi.org/10.1017/CBO9781139025683)

Harris, C. R., Millman, K. J., van der Walt, S. J., et al. 2020, *Nature*, 585, 357, doi: [10.1038/s41586-020-2649-2](https://doi.org/10.1038/s41586-020-2649-2)

Hofgartner, J. D., Buratti, B. J., Hayne, P. O., & Young, L. A. 2019, *Icarus*, 334, 52, doi: [10.1016/j.icarus.2018.10.028](https://doi.org/10.1016/j.icarus.2018.10.028)

Hromakina, T. A., Belskaya, I. N., Krugly, Y. N., et al. 2019, *A&A*, 625, A46, doi: [10.1051/0004-6361/201935274](https://doi.org/10.1051/0004-6361/201935274)

Hudson, R. L., Ferrante, R. F., & Moore, M. H. 2014a, *Icarus*, 228, 276, doi: [10.1016/j.icarus.2013.08.029](https://doi.org/10.1016/j.icarus.2013.08.029)

Hudson, R. L., Gerakines, P. A., & Moore, M. H. 2014b, *Icarus*, 243, 148, doi: [10.1016/j.icarus.2014.09.001](https://doi.org/10.1016/j.icarus.2014.09.001)

Hunter, J. D. 2007, *Computing in Science and Engineering*, 9, 90, doi: [10.1109/MCSE.2007.55](https://doi.org/10.1109/MCSE.2007.55)

Kiss, C., Müller, T. G., Farkas-Takács, A., et al. 2024, *ApJL*, 976, L9, doi: [10.3847/2041-8213/ad8dcb](https://doi.org/10.3847/2041-8213/ad8dcb)

Küppers, M., O'Rourke, L., Bockelée-Morvan, D., et al. 2014, *Nature*, 505, 525, doi: [10.1038/nature12918](https://doi.org/10.1038/nature12918)

Lellouch, E., Wong, I., Lavvas, P., et al. 2025, *A&A*, 696, A147, doi: [10.1051/0004-6361/202453619](https://doi.org/10.1051/0004-6361/202453619)

- Lippi, M., Villanueva, G. L., Mumma, M. J., & Faggi, S. 2021, *AJ*, 162, 74, doi: [10.3847/1538-3881/abfdb7](https://doi.org/10.3847/1538-3881/abfdb7)
- Molpeceres, G., Satorre, M. A., Ortigoso, J., et al. 2016, *ApJ*, 825, 156, doi: [10.3847/0004-637X/825/2/156](https://doi.org/10.3847/0004-637X/825/2/156)
- Mommert, M., p. Kelley, M. S., de Val-Borro, M., et al. 2019, *Journal of Open Source Software*, 4, 1426, doi: [10.21105/joss.01426](https://doi.org/10.21105/joss.01426)
- Moore, M. H., & Hudson, R. L. 1998, *Icarus*, 135, 518, doi: [10.1006/icar.1998.5996](https://doi.org/10.1006/icar.1998.5996)
- Mousis, O., Werlen, A., Benest Couzinou, T., & Schneeberger, A. 2025, *ApJL*, 983, L12, doi: [10.3847/2041-8213/adc134](https://doi.org/10.3847/2041-8213/adc134)
- Müller, D. R., Altwegg, K., Berthelier, J. J., et al. 2022, *A&A*, 662, A69, doi: [10.1051/0004-6361/202142922](https://doi.org/10.1051/0004-6361/202142922)
- Ortiz, J. L., Sicardy, B., Braga-Ribas, F., et al. 2012, *Nature*, 491, 566, doi: [10.1038/nature11597](https://doi.org/10.1038/nature11597)
- Pinilla-Alonso, N., Licandro, J., Brunetto, R., et al. 2024, *A&A*, 692, L11, doi: [10.1051/0004-6361/202450124](https://doi.org/10.1051/0004-6361/202450124)
- Protopapa, S., Grundy, W. M., Reuter, D. C., et al. 2017, *Icarus*, 287, 218, doi: [10.1016/j.icarus.2016.11.028](https://doi.org/10.1016/j.icarus.2016.11.028)
- Protopapa, S., Olkin, C. B., Grundy, W. M., et al. 2020, *AJ*, 159, 74, doi: [10.3847/1538-3881/ab5e82](https://doi.org/10.3847/1538-3881/ab5e82)
- Protopapa, S., Raut, U., Wong, I., et al. 2024, *Nature Communications*, 15, 8247, doi: [10.1038/s41467-024-51826-4](https://doi.org/10.1038/s41467-024-51826-4)
- Qasim, D., Chuang, K. J., Fedoseev, G., et al. 2018, *A&A*, 612, A83, doi: [10.1051/0004-6361/201732355](https://doi.org/10.1051/0004-6361/201732355)
- Rauscher, B. J. 2024, *PASP*, 136, 015001, doi: [10.1088/1538-3873/ad1b36](https://doi.org/10.1088/1538-3873/ad1b36)
- Roth, N. X., Milam, S. N., Cordiner, M. A., et al. 2025, *ApJL*, 986, L22, doi: [10.3847/2041-8213/add526](https://doi.org/10.3847/2041-8213/add526)
- Schaller, E. L., & Brown, M. E. 2007, *ApJL*, 659, L61, doi: [10.1086/516709](https://doi.org/10.1086/516709)
- Strobel, D. F. 2021, in *The Pluto System After New Horizons*, ed. S. A. Stern, J. M. Moore, W. M. Grundy, L. A. Young, & R. P. Binzel, 363–377, doi: [10.2458/azu_uapress.9780816540945-ch015](https://doi.org/10.2458/azu_uapress.9780816540945-ch015)
- Trotta, F. 1996, PhD thesis, -
- Verbiscer, A. J., Helfenstein, P., Porter, S. B., et al. 2022, *PSJ*, 3, 95, doi: [10.3847/PSJ/ac63a6](https://doi.org/10.3847/PSJ/ac63a6)
- Villanueva, G. L., Smith, M. D., Protopapa, S., Faggi, S., & Mandell, A. M. 2018, *JQSRT*, 217, 86, doi: [10.1016/j.jqsrt.2018.05.023](https://doi.org/10.1016/j.jqsrt.2018.05.023)
- Villanueva, G. L., Hammel, H. B., Milam, S. N., et al. 2023, *Nature Astronomy*, 7, 1056, doi: [10.1038/s41550-023-02009-6](https://doi.org/10.1038/s41550-023-02009-6)
- Virtanen, P., Gommers, R., Oliphant, T. E., et al. 2020, *Nature Methods*, 17, 261, doi: [10.1038/s41592-019-0686-2](https://doi.org/10.1038/s41592-019-0686-2)
- Wada, A., Mochizuki, N., & Hiraoka, K. 2006, *The Astrophysical Journal*, 644, 300, doi: [10.1086/503380](https://doi.org/10.1086/503380)
- Wallis, M. K., & MacPherson, A. K. 1981, *A&A*, 98, 45
- Wong, I., Protopapa, S., Holler, B., et al. 2024a, in *AGU Fall Meeting Abstracts*, Vol. 2024, P23G–03
- Wong, I., Brown, M. E., Emery, J. P., et al. 2024b, *PSJ*, 5, 87, doi: [10.3847/PSJ/ad2fc3](https://doi.org/10.3847/PSJ/ad2fc3)
- Young, L. A. 2013, *ApJL*, 766, L22, doi: [10.1088/2041-8205/766/2/L22](https://doi.org/10.1088/2041-8205/766/2/L22)